POLITECNICO DI TORINO

Master degree in Physics of Complex Systems

Master degree thesis

First Order Phase Transitions and Instabilities in Dipolar Lattice Bosons

Supervisors

Prof. Barbara Capogrosso Sansone
Prof. Vittorio Penna

Author

Stefano Peaquin

March 2026

Abstract

Dipolar bosons trapped in optical lattices represent an important subject in condensed matter physics due to their wide range of applications in quantum technologies and the potential to be used as quantum simulator to study more complex strongly-correlated systems. The presence of long-range and anisotropic dipolar interactions makes these systems very good candidates to realize exotic states of matter and study quantum phase transitions.

In this thesis, we consider a system of ultracold bosons confined into a two-dimensional square optical lattice and interacting via dipole-dipole interaction. Starting from the zero temperature phase diagram and the results obtained in the draft paper [1], we aim to extend the description to finite temperatures to understand the role of thermal fluctuations. We mainly focus on the range of parameters corresponding to the instability region found in [1], where large discontinuities in the density profile of the system arise due to the presence of first order phase transitions. We also study the temperature dependent behavior of the checkerboard-superfluid transition observed in the ground state.

Our results show that temperature strongly enriches the behavior of the system in the instability region. We observe that, on the one hand, thermal fluctuations reduce the extension of this region of the phase diagram, on the other hand, they change the nature of density discontinuities.

Understanding the finite temperature behavior of a system is crucial for experimental studies and applications. The findings obtained within this dissertation are relevant for current experiments in the field of lattice dipolar bosons, such as [2]. The interesting results obtained in this thesis already suggest a qualitative finite temperature phase diagram in the parameter region studied and the possibility to use it as a thermometer for experimental applications. Further simulations are needed to make these predictions quantitative.

Acknowledgements

I am grateful to my supervisor prof. Barbara Capogrosso Sansone for having me guided and helped in these months. Her experience, patience and valuable advice played a fundamental role in the development of this work.

I also would like to thanks prof. Vittorio Penna for his availability and constant support during the thesis project.

Computational resources are provided by HPC@POLITO.

Contents

List of Figures

Acronyms

BEC Bose-Einstein Condensate

BH Bose-Hubbard

SF Superfluid

MI Mott Insulator

MC Monte Carlo

MCMC Markov Chain Monte Carlo

MetA Metropolis Algorithm

PIMC Path Integral Monte Carlo

WA Worm Algorithm

EBH Extended Bose-Hubbard

DDI Dipole-dipole interaction

CB Checkerboard

DSS Diagonal Stripe Solid

IP Incompressible Phase

PS Phase Separation

IR Instability Region

NF Normal Fluid

Introduction

Low temperature physics is a branch of physics which studies the behavior and the properties of physical systems at very low temperatures, close to zero Kelvin. Over the years, low temperature physics found great popularity because of the important discoveries of new quantum phenomena and exotic states of matter that arise only in these regimes of sufficiently low temperatures.

Formally, low temperature physics began in the early 20th century when, in 1908, Heike Kamerlingh Onnes liquefied ^{4}He, a bosonic isotope of helium. Some years later, in 1911, Onnes exploited the properties of liquid helium to cool mercury below the temperature of 4 Kelvin (K), observing, for the first time, *superconductivity*, namely a physical state characterized by an almost vanishing value of the resistivity in which currents can flow without dissipations.

The great discoveries accomplished by Onnes open the door to further studies and researches in the field of low temperature physics, in particular about liquid helium. The Dutch physicist Willem Hendrik Keesom and his group in Leiden were the first to observe an anomalous behavior in the properties of ^{4}He close to the temperature of 2 K. The profile of its specific heat, plotted as a function of temperature, shows a dramatic spike for a certain values of temperature with the characteristic shape of the Greek letter λ [3]. This strange behavior was clearly interpreted as the hallmark of a phase transition, the so called *lambda transition*. Such result evinced the presence of two different liquid phases for helium based on the temperature value with respect to a critical one T_λ, now known as 2.17 K. When $T > T_\lambda$, ^{4}He behaves as a normal fluid, called Helium I in the work by Keesom, while for $T < T_\lambda$, it changes its properties to enter into a new exotic phase, denoted as Helium II.

The features characterizing Helium II were then observed experimentally and reported in two independent works in 1938 by Pyotr Kapitza in Moscow [4], and by John F. Allen and Austin D. Misener in Toronto [5]. Both works highlight that, for $T < T_\lambda$, liquid helium shows interesting non-classical properties: it acquires a non-zero viscosity, leading to a frictionless flow, and an incredibly high thermal conductivity. It was Kapitza himself that, due to the analogy with superconductivity, introduced for the first time the term *superfluid* to describe the phase of liquid helium below the critical temperature T_λ.

After the experimental discovery of *superfluidity* in liquid helium different studies were developed with the aim to find a theoretical explanation about this newly discovered state of matter. In 1938, suggested by experimental results and by the bosonic nature of ^{4}He, Fritz London proposed that superfluidity was a macroscopic manifestation of the *Bose-Einstein condensation*. Bose-Einstein condensate, predicted by Einstein in 1925 starting from a pioneering paper by Satyendra Nath Bose [6], is a state of matter that is formed when a gas of non-interacting bosons is cooled to temperatures close to zero Kelvin. In such conditions, a large fraction of particles condensate to the lowest quantum state, leading to the appearance of macroscopic quantum effects. London intuitions inspired the well known *two-fluid model* introduced by Laszlo Tisza in 1938 and reformulated by Lev D. Landau in 1941 [7]. To explain the anomalous low temperatures behavior of helium the model states that the liquid can be thought as the result of two independent components: a superfluid component, that possesses zero viscosity and zero entropy, and a normal component that behaves like a normal fluid and carries entropy. The amount of one or the other component depends on the temperature at which we observe the system.

Despite the great theoretical work done by Tisza and Landau, the true connection between superfluidity and BEC was still unknown and unsure. Moreover, there was also the doubt if, a phenomenon apparently so similar to superfluidity like superconductivity, could be as well related to the Bose-Einstein condensation, despite the fermionic nature of the electrons that flow without resistance in a superconductor. The answer to these questions became clear years later. Firstly, Penrose and Onsager introduce a generalization of the BEC as *"off-diagonal long range order"* in the formalism of density matrix [3, 8]. In their work they showed the possibility to have a condensate fraction much smaller than the total mass and thus to extend the concept of Bose-Einstein condensation in the case of interacting systems, such as liquid helium. Secondly, in 1957, thanks to the work of Bardeen, Cooper and Schrieffer was introduced the first microscopic theory of *conventional superconductors*, the *BCS theory* [9]. The three physicists explained that, below a certain critical temperature, the collective lattice vibrations mediate an attractive interaction between electrons that form pairs, which behaves as bosonic quasiparticles. These quasiparticles, called *Cooper pairs*, condensate to the minimum energy quantum state, leading to an abrupt drop, from a finite value to zero, in the material resistivity. The ideas behind BCS theory and Cooper pairs were then experimentally confirmed in 1972, when superfluidity was observed in ^{3}He, a fermionic isotope of helium, at temperatures around 2 mK.

Thanks to these discoveries it was possible to conclude that both superfluidity and superconductivity are macroscopic realizations of the Bose-Einstein condensation in which an important fraction of particles condensate to the lowest energy state and whose behavior is dictated by quantum mechanical laws. However, it is important to highlight that superfluidity and superconductivity are not the same phenomenon as BEC, they are simply related to it. In fact, the typically strong interactions characterizing these states of matter are not present in the ideal gas analyzed by Einstein and Bose in their works.

Bose-Einstein condensation was finally obtained experimentally in 1995 by the group of Weiman and Cornell, using atoms of Rubidium $\left(^{87}\mathrm{Rb}\right)$ [10], and by the group of Ketterle with Sodium $\left(^{23}\mathrm{Na}\right)$ [11]. In both works, evaporative cooling techniques allowed to reach incredibly low temperatures and to observe the condensation of the particles into the lowest energy state. Years later, thanks to technological development, it was possible to create condensates with a large variety of atoms, including *dipolar bosons*, such as $^{52}\mathrm{Cr}$ and $^{164}\mathrm{Dy}$ [12, 13]. As we will discuss later, the possibility to obtain condensates with particles owning a permanent dipolar moment was crucial since the presence of a long range and anisotropic dipolar interaction supports the emergence of interesting new behaviors. After the experimental realization of Bose-Einstein condensation in dilute atomic gases, the field of ultracold atoms acquired a great popularity and an important number of researches began with the goal of deeply understand this class of systems.

A gas composed by cold particles can be classified as *weakly interacting* or *strongly interacting* based on the value of the ratio between the interaction energy among the particles of the gas, i.e. E_{int}, and their kinetic energy, i.e. E_{kin}. In general, in the case of a dilute gas, as we will see more in detail later, the diluteness condition implies a small value of the ratio E_{int}/E_{kin}, allowing to consider the system as weakly interacting. This latter type of systems can be entirely described analytically, by means of a mean field approach and a perturbative treatment of the small quantum fluctuations (see e.g. Ref. [14]). On the other hand, when the ratio E_{int}/E_{kin} starts to increase, the system enters in a regime in which particles correlations and their interactions play a crucial role in the description of the physical properties of the quantum gas. The greater complexity of the systems in these conditions makes their analytical treatment more difficult and, in general, numerical methods, such as quantum Monte Carlo and density matrix renormalization group, are used to investigate the interesting behavior of strongly interacting systems.

A possible way to achieve the strongly interacting regime consists of loading a weakly interacting Bose gas into an *optical lattice*. Optical lattices are periodic arrays of potential wells in 1, 2 or 3 dimensions that can be created by the superposition of two, or more, counter propagating laser beams [15, 16]. The strong confinement of bosons close to the minima of the optical potential leads to a strong reduction in the kinetic energy, i.e. in the tunneling process form one site to the other, of the particles. In this way, the ratio E_{int}/E_{kin} increases [17]. Optical lattices rapidly have become one of the most exploited tool for the analysis of strongly interacting systems because of their high versatility. In fact, by means of simple changes in the laser configuration, it is possible to change the depth of the potential minima, vary the spatial distance between two consecutive wells and also modify the geometry of the lattice itself. Moreover, optical lattices give the opportunity to generate clean potential landscape and ensure an high isolation of the system from the external environment.

Systems of ultracold bosonic atoms trapped in optical lattices are modeled by the famous *Bose-Hubbard model*. The model was introduced by Gersch and Knollmann in 1963 in the context of granular superconductors [18]. Later on, in the 1980s, it gained a large popularity since it was found to capture the essence of the superfluid-insulator transition, and thus, became a reference model in condensed matter physics for the description of a large number of systems, such as ultracold atoms in optical lattices.

The great regard arose around lattice bosons can be in part explained by their large number of possible applications in different fields concerning quantum technologies, like, for instance, interferometry [19] and quantum information processing [20]. However, the probably most fascinating quality of ultracold particles trapped in optical lattices is their potential to be exploited as *quantum simulator* to study the behavior of complex systems in condensed matter physics [21]. The versatility of optical lattices and their similarity with the actual lattice of a crystalline material make these tools the best candidates to study and experimentally realize different classes of Hamiltonians. Moreover, when particles own a permanent dipole moment, the presence of a long-range and anisotropic dipolar interaction allows for the onset of interesting and new behaviors which give rise to a wealth of exotic phases as well as more sophisticated applications in the field of quantum technologies.

Systems of strongly interacting dipolar bosons are the subject of the research work discussed in this dissertation. In this thesis, we consider a system of ultracold hard-core bosons confined into a two-dimensional square optical lattice and interacting via dipole-dipole interaction. This system can be efficiently modeled by the extended version of the Bose-Hubbard model, where, in addition to the standard kinetic energy term and on-site repulsive interaction, a further term is introduced in order to include the long range and anisotropic interaction between dipolar particles. In their draft work [1], Y. Hebib, C. Zhang and B. Capogrosso Sansone studied the same system at zero temperature and reported the phase diagram at half filling as a function of the strength of the dipole interaction V, and the angle θ between the dipole moments of the atoms, all aligned by an external electric field, and the spatial vertical direction. In the zero temperature phase diagram, based on the values of the parameters V and θ, the system can be found in different quantum phases, such as checkerboard, superfluid, diagonal stripe solid and an instability phase, where the average particles number undergoes a first order phase transition from empty-filled to fully-filled lattice as a function of the chemical potential, that is, no filling factors beside zero and one are stable. Starting from the results in [1], our goal is to understand how the behavior of the system, specifically within the instability region, changes when we consider a temperature different from zero, i.e when thermal fluctuations are included.

Firstly, we fix the value of the dipolar interaction strength V and investigate the behavior of the system for the range of angles θ belonging to the instability region. Here, not only we study the stability of the system at half filling as a function of T and θ, as done in [1], but we extend the analysis to all possible densities that the system can achieve. We observe that, as temperature increases, the critical angle that divides the stable region from the instable one moves toward larger values of θ. More interestingly, we discover a more intricate instability region in which first order phase transitions occur between filling factors other than 0 and 1, depending on temperature and polarization angle. We conclude the finite temperature analysis by studying the melting of the checkerboard phase at fixed V as a function of the temperature.

Understanding the system behavior at finite temperature is important for experimental researches and applications which cannot be carried on at zero temperature. The results of this work are relevant for current experimental studies in the field of lattice dipolar bosons, such as [2].

The complexity of the system Hamiltonian for this class of systems prevents an analytical treatment of the problem. For this reason, all the results reported in this dissertation are based on quantum Monte Carlo by the worm algorithm, a powerful generalization of the well known class of path integral Monte Carlo methods introduced by N. Prokof'ev *et al.* in [22].

Overview

The structure and the topics discussed in this dissertation can be summarized as follows.

Chapter 1 is divided into two parts. In the first we present the model considered, i.e. ultracold atomic gases, introduce the concept of optical lattices and conclude with a brief review of the properties of a single particle moving in a periodic potential. The second part is devoted to the description of the Bose-Hubbard model. After the derivation of the model, we focus on the Mott-insulator to superfluid transition.

Chapter 2 is dedicated to the method used for the thesis. We start with a review of classical Monte Carlo methods and Metropolis algorithm and then, introduce the path integral Monte Carlo approach and the worm algorithm.

Chapter 3 focus on the properties of dipolar bosons and their description. We briefly discuss the theory behind dipole-dipole interaction and introduce the extended version of the Bose-Hubbard model that allows to model the behavior of lattice dipolar bosons. We end the chapter with some examples of numerical studies on the behavior of dipolar bosons trapped in optical lattices, with special concern on [1], whose results represent the starting point for the numerical analysis done in this dissertation.

Chapter 4 presents our numerical results. Starting from the zero temperature findings of paper [1] we extend the description for $T > 0$. The chapter is divided into two part. The first and main part is dedicated to the study of the instability region, while the second part investigates the melting of the CB phase as a function of temperature.

Chapter 5 contains the conclusion and the outlook of the dissertations. After a brief recap of the results find within this work, we describe the next steps needed to conclude the work started in this dissertation and describe some practical applications in which they can be involved.

Chapter 1

Ultracold Atomic Gases in Optical Lattices

In this chapter, we will discuss some of the main results in the field of ultracold atoms trapped in optical lattices. Moreover, we will describe the model used in condensed matter physics to characterize the behavior of interacting bosons on a lattice: the Bose-Hubbard model.

1.1 Physics of ultracold atoms

The achievement of Bose-Einstein condensation in ultracold dilute gasses has played a fundamental role in atomic and molecular physics. It has allowed to open a new chapter in which the main players are no longer the single particles composing the gas, but instead the particle statistics and their interactions [15]. As a consequence, the research field concerning ultracold gasses of particles has become more and more relevant, leading to new interesting discoveries.

Initially, the attention was directed to the class of the so called weakly interacting systems. The weakly interacting condition strongly simplifies the analysis of such systems and it is closely related to the diluteness of the gas. In order to better understand the last sentence and to state what is the actual range of physical parameters for which one can consider a system as weakly interacting, let us consider a three dimensional gas of volume V with N particles. The system is said to be dilute if

$$d >> r_0, \tag{1.1}$$

where r_0 is the range of interatomic forces and $d^3 = 1/n$ is the volume per particle with $n = N/V$. In such conditions, it is reasonable to consider only two-particle interactions, while the simultaneous interaction of three or more particles can be safely neglected. Moreover, when condition (1.1) holds and we are dealing with low temperatures, i.e. temperatures lower than the critical temperature for the BEC, standard scattering theory (see e.g. [23]) states that the scattering amplitude, namely the parameter that characterizes the behavior of the relative motion wavefunction of the two particles involved in the collision, only depends on the s-wave scattering length, denoted by a_s. In this regard, the diluteness condition (1.1) is typically expressed as

$$n^{\frac{1}{3}} a_s << 1, \tag{1.2}$$

where a_s plays the role of the effective range of the interaction forces. The form (1.2) of the diluteness condition shows that the large separation between particles that occurs in a dilute system makes it more likely for interactions to be weak.

As previously anticipated, the presence of weak interactions highly simplifies the analysis of the system allowing, in general, for a complete analytical treatment of the problem. In fact, in this scenario, the many-body properties of the system can be reduced to an effective single particle description through a macroscopic wavefunction [15]. The behavior of the latter and its time evolution are governed by a non linear version of the Schrödinger equation, namely the well known Gross-Pitaevskii equation, in which the non linear term has been introduced in order to take into account the interaction between the particles of the gas.

Over the years, as reported in Ref. [15], the large interest about ultracold atoms leads to two new crucial developments that considerably enlarged the range of physics which is accessible with dilute ultracold gases:

- the ability to exploit Feshbach resonance to tune the scattering length a_s between the particles of the gas [24];
- the possibility to confine the cold atoms in a region of reduced dimensionality or in a periodic lattice through the application of optical potentials [25].

Both discoveries allow us to study a new class of systems, the so-called strongly-correlated systems. In fact, they remove the possibility of studying the system as a collection of weakly interacting particles governed by a single macroscopic wavefunction, also for extreme dilute gasses. This new class of strongly interacting systems has rapidly become very popular and, due to their complexity, they represent one of the major challenges in the field of condensed matter physics. Due to the practical impossibility to study the behavior of these systems analytically, they are typically treated through numerical approaches, such as quantum Monte Carlo simulations or density matrix renormalization group techniques.

Let us now focus more in detail on one of the two developments previously mentioned: the optical lattices.

1.1.1 Optical lattices

Optical lattices are periodic arrays of potential wells in 1,2 or 3 spatial dimensions. The simplest way in which optical lattices are created is the superposition of two, or more, counter propagating laser beams [15, 16].

For a one-dimensional system, a periodic potential is generated by overlapping two counter propagating laser beams. Due to the interference process between the beams, an optical standing wave with period $\lambda/2$ is formed and allows trapping the atoms in a periodic structure. Mathematically, the periodic potential generated can be described as

$$V(x) = V_0 \sin^2(kx), \tag{1.3}$$

where $k = 2\pi/\lambda = \pi/a$ is the wavevector, a is the lattice space separation, i.e. the distance between two consecutive minima of the potential, and V_0 is the depth of the lattice wells. Both the parameters a and V_0 of the optical lattice can be easily tuned by varying respectively the period and the intensity of the laser beams.

In higher dimensions, optical lattices are simply obtained by superimposing more laser beams. For example, in the case of a three dimensional lattice, three orthogonal optical standing waves have to be overlapped, each of them generated by the superposition of two counter-propagating laser beams. The total potential will read

$$V(\mathbf{r}) = V_{0,x} \sin^2(k_x x) + V_{0,y} \sin^2(k_y y) + V_{0,z} \sin^2(k_z z), \tag{1.4}$$

where, as seen before, the lattice depth in each of the three directions is determined by the intensity of the corresponding laser beams.

The possibility to investigate the properties of strongly interacting systems is one of the greatest advantages of optical lattices. Lasers are very versatile and highly controllable experimental tools used to manipulate and confine atoms. It follows, that they give the opportunity to modify, in a relatively easy way, the features of the lattice by a change in the lasers configuration. Not only is it possible to vary the depth of the wells by increasing or decreasing the intensity of the laser beams, but it is also possible to achieve different lattice geometry (e.g. triangular lattice in two dimensions, etc.) by simply changing the setup and the directions of the lasers configuration. Another great advantage of optical lattices is the possibility to create potential traps for different internal states of the atoms. This can be achieved by manipulating the polarization of the light, which acts differently based on the internal states [17].

To sum up, optical lattices can experimentally realize different classes of Hamiltonians in a controlled manner. In this regard, ultracold atoms in optical lattices are typically considered as quantum simulators, i.e. highly controllable quantum systems that exploit their own properties to mimic and reproduce the behavior of other, more complex, quantum systems.

1.1.2 Ultracold bosons trapped in optical lattices

In the last subsection related to the physics of ultracold atoms in optical lattices we aim to conclude by a brief review about the behavior of quantum particles exposed to a periodic potential. For the sake of simplicity, we will consider the one dimensional case, but a generalization to higher dimensions can be done straightforwardly. We use [17, 26] as references.

Bloch theorem and Bloch bands

Solid state physics shows that the presence of an external periodic potential destroys the continuous energy spectrum of the system exposed to it by generating a band structure in the energy spectrum where forbidden energy regions, called gaps, are opened between the accessible energy bands.

To better clarify this concept, let us consider the Hamiltonian, in the Schrödinger formalism, of a gas of non interacting particles exposed to an external periodic potential, namely

$$\hat{H} = \sum_{i=1}^{N} \frac{\hat{p}_i^2}{2m} + \sum_{i=1}^{N} V(\hat{x}_i) = \sum_{i=1}^{N} \hat{H}_i, \tag{1.5}$$

where N is the total number of particles, m is their mass, $\hat{x}_i$ and $\hat{p}_i$ are respectively the position and momentum operator of the i-th particle and $V(\hat{x}_i)$ is the potential acting on the i-th particle. We denote by a the spatial period of the potential, i.e. $V(x+a) = V(x)$. Since the Hamiltonian (1.5) can be written as a sum of commuting single particle Hamiltonians, the full quantum problem can be reduced to solve the eigenvalue problem for the single particle Hamiltonian $\hat{H}_i$, which we can write in the form

$$\hat{H}\phi_\nu(x) = E_\nu \phi_\nu(x), \tag{1.6}$$

where we indicate with ν the multi-index for the set of quantum numbers labeling the possible solutions of the problem and we drop, for simplicity, the subscript i in the single particle Hamiltonian. The solution of the eigenvalue problem (1.6) is given by the famous Bloch theorem. The latter states that the wavefunction that describes a particle exposed to a periodic potential can be expressed as a planewave modulated by a periodic function $u(x)$, explicitly

$$\phi_{k,n}(x) = e^{ikx} u(x), \tag{1.7}$$

where the function $u(x)$ has a period that coincides with the one of the potential $V(x)$, i.e. a, and is called Bloch function.

The eigenstates (1.7) characterizing the behavior of the particle are labeled by two distinct quantum numbers: k and n. The first, k, is associated with the discrete translational invariance of the lattice and defines the allowed states in an energy band. When multiplied by $\hbar$, the quantum number k is called quasimomentum. The second, n, is the so called band index. The latter indicates which energy band the solution $\phi_{k,n}$ refers to.

To understand why n is the quantum number labeling the energy bands in the spectrum, let us consider the Schrödinger equation for the Bloch function $u(x)$. Plugging the Bloch wavefunction (1.7) into the eigenvalue problem (1.6) one obtains

$$\left(\frac{\hbar^2}{2m}\left(k - i\frac{\mathrm{d}}{\mathrm{d}x}\right)^2 + V(x)\right)u_{k,n}(x) = E_{n,k}u_{n.k}(x). \tag{1.8}$$

The index n stems from the fact that, for a given value of k there exist multiple solutions of the eigenvalue problem (1.8). In other words, for the same value of quasimomentum, one can identify a set of equations, labeled by n, whose solutions describe a family of energy eigenvalues $E_{k,n}$. Moreover, one can show that, for a lattice with a large number of sites, the energy eigenvalues become almost continuous functions of k, which we can denote as $E_n(k)$, with the same periodicity of the reciprocal lattice vectors, i.e. $2\pi/a$, in the momentum space. For this reason, they present minimal and maximal values and can thus be considered as the energy profile of the bands in the single particle spectrum.

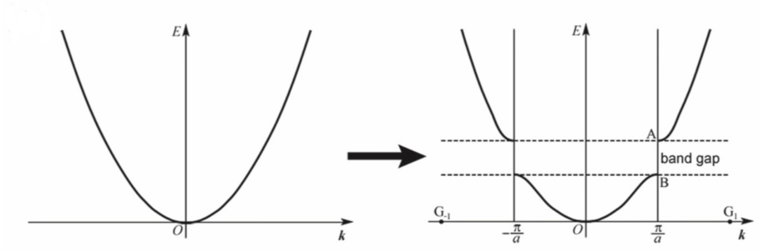

Figure 1.1: Dispersion relation for a free particle (left panel) and for a particle moving in a periodic lattice (right panel). The presence of a periodic potential leads to the creation of a band structure in the spectrum where forbidden energy gaps appear. The figure is borrowed from Ref [27].

To conclude, in figure 1.1 is reported the profile of the dispersion relation, i.e. the behavior of the energy as a function of the wavevector, for a free particle (left panel) and for a particle exposed to a weak periodic potential of period a (right panel) both in one dimension. As one can see, the presence of the periodic lattice leads to the formation of a band structure in the spectrum, where available energy regions are separated by forbidden energy gaps.

Wannier functions and tight binding approximation

The Wannier functions are an orthonormal basis of states that can be formally defined by taking the Fourier transform of the Bloch wavefunctions (1.7). Explicitly one gets

$$w_n(x - x_j) = \frac{1}{\sqrt{N}}\sum_k e^{-ikx_j}\phi_{k,n}(x), \tag{1.9}$$

where n is still the quantum number associated to the energy band while j, that replaces the quantum number k of the Bloch functions, labels the sites of the lattice.

Exploiting these results, we can write the single particle wavefunction as a superposition of Wannier states, namely

$$\psi(x,t) = \sum_{n,j} c_j^{(n)}(t) w_n(x - x_j), \tag{1.10}$$

where $c_j^{(n)}(t)$ is the weight with which the basis element $w_n(x - x_j)$ contributes to the superposition.

The description in terms of Wannier functions becomes more appropriate the more the lattice depth is large. In fact, working with optical lattices in the limit of low temperature, already for moderate lattice depth, the separation between the lowest energy band and the excited states is large. It follows, that the ultracold bosons trapped in the optical lattice tend to occupy the lowest energy level of each potential well localized at $x = ja$ with $j = 1, \ldots, M$ and M the total number of lattice sites, leaving the excited states empty. In this scenario, in which particles are strongly localized at the different lattice sites, only the contribution from the lower band, i.e. $n = 0$, matters. In this regard expression (1.10) can be recast as

$$\psi(x,t) = \sum_{j} c_j^{(0)}(t) w_0(x - x_j), \tag{1.11}$$

in which only the set of Wannier functions associated to the $n = 0$ energy band have been introduced in the summation. Moreover, one can show that, in these conditions, the Wannier function $w_0(x - x_j)$ tends to the ground state of an harmonic oscillator associated with the j-th well.

In general, when the overlap between Wannier states localized at different lattice sites can be considered as a small correction to the picture of isolated particles, the well known tight binding approximation can be used. The tight binding approximation is a famous method in solid state physics that allows to determine the band structure for particles moving in a periodic lattice in the regime in which the particles are strongly localized in the minima of the potential. In fact, the idea behind this approximation is to consider the initial wavefunctions as the atomic ones and then, try to correct the results by introducing the effect of the other lattice sites as a perturbation. It follows, that this method is typically used to describe the energy bands of materials with localized d-orbitals, such as transition metals and insulators. The concepts of Wannier functions and tight binding approximation will become very useful in the following sections where we will derive the Hamiltonian of the Bose-Hubbard model.

1.2 The Bose-Hubbard model

The Bose-Hubbard model, developed in the early 1960's, is the simplest model that allows to describe interacting bosons on a lattice. The structure of the model is characterized by a kinetic energy term, which accounts for the hopping of the particles within the sites of the lattice, and a potential energy term, which takes into account the density-density repulsion between bosons in the same well. The competition between these two terms is responsible for the interesting properties of bosonic systems.

Over the years the Bose-Hubbard model has been used to study different systems in condensed matter theory, such as the critical properties of Helium-4 absorbed in porous media [28, 29], superconductor to insulator transition in Josephson junction arrays [28, 30], phonons in lattices [31] and cold atoms in optical lattices [32]. The possible approaches used for the solution of the model are both analytical and numerical. On the one hand, the most used analytical techniques are: mean-field [33, 34], renormalization group approach [28] and strong coupling expansion [35, 36]. On the other hand, numerical methods such as quantum Monte Carlo [37, 38, 39] and density matrix renormalization group techniques [40, 41] are widely exploited.

Moreover, as we will discuss at the end of the chapter, the BH Hamiltonian predicts a quantum phase transition from a superfluid to a Mott-insulator state. The transition was observed experimentally for the first time using ^{87}Rb atoms confined in a three-dimensional optical lattice [25].

1.2.1 Derivation of the Bose-Hubbard Hamiltonian

The aim of this section is to derive the Hamiltonian for the Bose-Hubbard model. For this purpose, we will follow the analysis done in [32, 42]. Let us start by the second-quantized Hamiltonian describing a Bose gas of interacting particles in the presence of an external potential

$$\begin{aligned} \hat{\mathcal{H}} = & \int \mathrm{d}\mathbf{r}\, \hat{\psi}^\dagger(\mathbf{r}) \left[-\frac{\hbar^2}{2m} \nabla^2 + \mathcal{V}(\mathbf{r}) \right] \hat{\psi}(\mathbf{r}) + \\ & + \frac{1}{2} \int \int \mathrm{d}\mathbf{r}\, \mathrm{d}\mathbf{s}\, \hat{\psi}^\dagger(\mathbf{r}) \hat{\psi}^\dagger(\mathbf{s}) U(\mathbf{r}-\mathbf{s}) \hat{\psi}(\mathbf{s}) \hat{\psi}(\mathbf{r}), \end{aligned} \tag{1.12}$$

whit $\hat{\psi}(\mathbf{r})$ a bosonic field operator, $\mathcal{V}(\mathbf{r}) = V_p(\mathbf{r}) + V_t(\mathbf{r})$ the external potential composed by two different contributions: the periodic potential of the optical lattice V_p responsible for the occurrence of the local minima and a slowly varying trapping potential V_t confining the gas in a finite spatial domain, and $U(\mathbf{r}-\mathbf{s})$ the interaction potential.

In principle, the interaction potential U can be a complicated function of the position of the two particles involved in the interaction. However, the latter can be simplified by considering the assumption of a dilute gas of slow bosons. In fact, in these conditions, scattering theory (see e.g. [23]) states that the relative motion wavefunction describing the particle after the collision reads

$$\phi(\mathbf{R}) = e^{i\mathbf{kR}} + f(\theta)\tfrac{e^{i\mathbf{kR}}}{R} \qquad \text{where} \quad \mathbf{R} = \mathbf{r} - \mathbf{s},$$

with a scattering amplitudes given by

$$f(\theta) = \textstyle\sum_{l=0}^{\infty} s_l P_l(\cos\theta) \simeq s_0 =: -a_s,$$

where θ is the scattering angle and $P_l(\cos\theta)$ is the Legendre polynomial of order l. In other words, we evince that, in this regime, only the zero order term, a_s, contributes to the scattering function. This contribution is called s-waves scattering length and it is independent of the angle θ. In this regard, by exploiting the Born approximation for the scattering length of a dilute gas of slow bosons,

$$f(\theta) = -\frac{m}{4\pi\hbar^2}\int \mathrm{d}\mathbf{R}\, U(\mathbf{R}), \tag{1.13}$$

one is able to get the Fourier transform of the potential as

$$U(\mathbf{Q}) = \int \mathrm{d}\mathbf{R}\, U(\mathbf{R}) e^{-i\mathbf{QR}} \simeq \int \mathrm{d}\mathbf{R}\, U(\mathbf{R}) \simeq \frac{4\pi a_s \hbar^2}{m}, \tag{1.14}$$

that leads to a pseudopotential approximation

$$U(\mathbf{r}-\mathbf{s}) = \frac{4\pi a_s\hbar^2}{m}\delta^3(\mathbf{r}-\mathbf{s}). \tag{1.15}$$

In summary, in the case of a dilute gas of slow bosons, the interaction potential can be approximated with an effective contact interaction of the form (1.15). Using the latter result, the Hamiltonian (1.12) can be recast as

$$\hat{\mathcal{H}} = \int \mathrm{d}\mathbf{r}\left[\hat{\psi}^\dagger(\mathbf{r})\left(-\frac{\hbar^2}{2m}\nabla^2 + \mathcal{V}(\mathbf{r})\right)\hat{\psi}(\mathbf{r}) + \frac{2\pi a_s\hbar^2}{m}\left(\hat{\psi}^\dagger(\mathbf{r})\right)^2\left(\hat{\psi}(\mathbf{r})\right)^2\right]. \tag{1.16}$$

For what concern the term V_p we can chose the simplest form for an optical potential in three spatial dimensions, namely

$$V_p(\mathbf{r}) = \sum_{i=1}^{3} V_{0,i}\sin^2(kx_i), \tag{1.17}$$

where $k = 2\pi/\lambda$ is the wavevector, λ is the wavelength of the laser light and V_0 is proportional to the laser intensity. The resulting lattice has a period $a = \lambda/2$.

In this scenario, the field operators can always be expanded in the basis of Bloch functions $\phi_{n,k}(\mathbf{r})$

$$\hat{\psi}(\mathbf{r}) = \sum_{n,k} \hat{a}_{n,k}\phi_{n,k}(\mathbf{r}), \tag{1.18}$$

where n is the band index, k is the momentum index and $\hat{a}_{n,k}$ is the bosonic annihilation operator associated to n and k. However, as we highlighted in the previous section, it is more convenient to switch to the orthonormal Wannier orbital basis $w_n(\mathbf{r}-\mathbf{r}_i)$, namely

$$\hat{\psi}(\mathbf{r}) = \sum_{n,i} \hat{a}_{n,i} w_n(\mathbf{r}-\mathbf{r}_i), \tag{1.19}$$

where i is the index labeling the lattice site. Moreover, for sufficiently deep optical potentials, and at low temperatures, the band gap between the lowest and the first excited band may be large enough, so that the second and higher energy bands will practically not be populated and can be disregarded. It follows, that expression (1.19) for the field operator simplifies as

$$\hat{\psi}(\mathbf{r}) = \sum_{i} \hat{a}_{i} w_0(\mathbf{r}-\mathbf{r}_i), \tag{1.20}$$

where $w_0(\mathbf{r}-\mathbf{r}_i)$ is the Wannier function for the lowest energy band.

Introducing the latter expansion in the field Hamiltonian (1.16) and considering only tunneling between nearest neighbors sites, one obtains the Bose-Hubbard Hamiltonian

$$\hat{H}_{BH} = -J \sum_{\langle i,j \rangle} \hat{a}_i^{\dagger} \hat{a}_j + \frac{U}{2} \sum_i \hat{n}_i(\hat{n}_i - 1) + \sum_i \varepsilon_i \hat{n}_i, \tag{1.21}$$

where $\hat{n}_i = \hat{a}_i^{\dagger}\hat{a}_i$ is the number density operator at site i and the symbol $\langle i,j \rangle$ stands for pairs of nearest neighbors. The parameter obtained from the calculation are defined as follows

$$\begin{aligned}
U &= \frac{4\pi a_s \hbar^2}{m} \int d\mathbf{r}\, |w_0(\mathbf{r})|^4 \\
J &= \int d\mathbf{r}\, w_0(\mathbf{r}-\mathbf{r}_i) \Big(-\frac{\hbar^2}{2m}\nabla^2 + V_p(\mathbf{r}) \Big) w_0(\mathbf{r}-\mathbf{r}_j) \\
\varepsilon_i &= \int d\mathbf{r}\, V_t(\mathbf{r}) |w_0(\mathbf{r}-\mathbf{r}_i)|^2
\end{aligned}$$

where U measures the strength of the repulsion between two atoms occupying the same lattice site; J is the hopping amplitude between adjacent sites, i.e. it is a measure of the kinetic energy of the system; ε_i describes an energy offset of each lattice site, due for example to the presence of the trapping potential V_t. A graphical representation of the meaning of the parameters of the BH model is reported in picture 1.2 (a).

Figure 1.2 (b) describes instead the behavior of the hopping matrix element J and the onsite interaction U as a function of the lattice amplitude V_0. Energies are measured in units of recoiled energies $E_R = \frac{\hbar^2 k^2}{2m}$. As one can notice from the picture the dependence of the two parameters is not the same. In particular

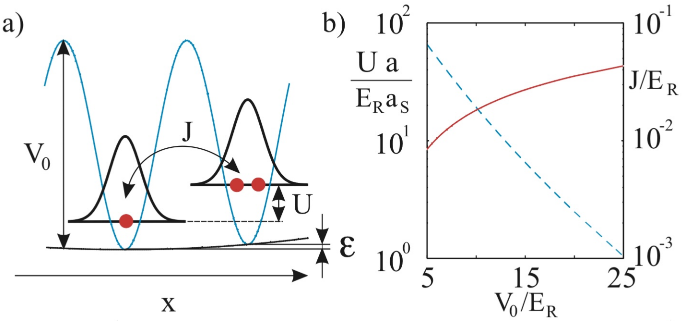

Figure 1.2: In panel a) is reported a graphical representation of the meaning of the parameters present in the BH model; in b) the behavior of U (solid line, axis on the left-hand side of the graph) and J (dashed line, axis on the right-hand side of the graph) as a function of the potential amplitude V_0. The figure is borrowed from Ref [32].

one can show that the hopping parameter depends exponentially on V_0, while the onsite interaction depends algebraically. This result is crucial since highlight the possibility of tuning J and U independently by varying V_0.

1.2.2 The Bose-Hubbard model in the Grand Canonical Ensemble

In the grand canonical ensemble the number of particles is not a conserved quantity, since the system can exchange both energy and particles with an external reservoir. In this context, one has to deal with a further thermodynamical variable: the chemical potential μ. The Hamiltonian of the Bose-Hubbard model thus becomes

$$\hat{\mathcal{H}}_{BH} = \hat{H}_{BH} - \mu\hat{N} = -J\sum_{\langle i,j\rangle}\hat{a}_i^{\dagger}\hat{a}_j + \frac{U}{2}\sum_i \hat{n}_i(\hat{n}_i - 1) - \sum_i \mu_i\hat{n}_i, \tag{1.22}$$

where $\hat{N} = \sum_i \hat{n}_i$ is the total bosons number and we introduce $\mu_i = \mu - \varepsilon_i$. The chemical potential μ can be interpreted as a Lagrange multiplier that fixes the mean number of bosons in the system. The variable μ_i can instead be considered as a sort of local chemical potential that can change from a site to the other based on the variations of the trapping potential V_t.

1.2.3 Mott-insulator to Superfluid Transition

The Bose Hubbard model has been widely studied in the last thirty years owing to the fact that it presents a quantum phase transition at zero temperature. A quantum phase transition is not caused by the competition between inner energy and entropy as a classical phase transition, since at zero-temperature thermal fluctuations are not present. Nevertheless, in quantum systems, fluctuations are present even at zero temperature, due to the Heisenberg's uncertainty principle. In some cases, these quantum fluctuations may be strong enough to drive a transition from one phase to another. In other words, by varying some parameters of the model, the ground state of the system can go through a macroscopic change of its properties [25].

For the Bose-Hubbard model the transition can be thought as a competition between the kinetic energy term, that tends to delocalize the particles through the hopping process, and the potential energy term, that instead tends to localize the particles in the lattice in order to minimize the repulsive interaction between them. At zero temperature, this competition leads to the well known quantum transition from a superfluid state to a Mott insulator one [28].

The SF-MI transition has been studied both theoretically and numerically (see e.g. [28, 40]) and, thanks to the development of the experimental techniques, it was observed for the first time by M. Greiner *et al.* exploiting atoms of rubidium-87 trapped in an optical three-dimensional lattice [25].

To study the zero-temperature phase diagram of the BH model one usually refers to the operator $\hat{H}_{BH} - \mu\hat{N}$, where $\hat{N} = \sum_i \hat{n}_i$ is the total bosons number. In particular, the crucial parameters that allow to describe the transition for the model, and are thus used to label the axis of the phase diagram, are: J/U and μ/U. The latter is reported in figure 1.3.

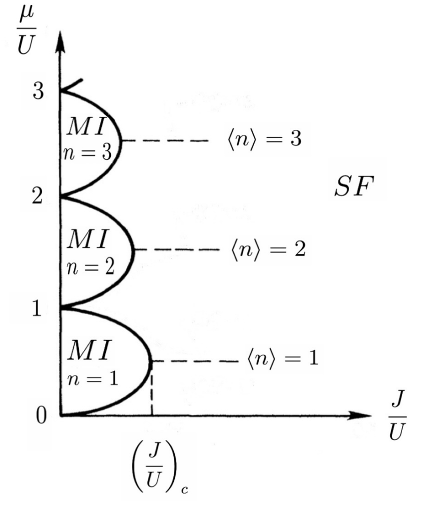

Figure 1.3: Phase diagram at zero temperature of the Bose-Hubbard model. The points of the phase diagram inside the lobes identify the Mott insulator phase, while the region outside the lobes corresponds to the superfluid state. The value n is defined as the total number of particles divided by the number of wells. The figure is adapted from [28].

The phase diagram is characterized by a typical lobe structure, with the MI phase inside the lobes and the SF one outside. There is one lobe, denoted as $\mathcal{L}_n$, for each integer filling factor n.

Let us now focus on the description of the two phases, trying, with the help of [25, 28], to highlight their main properties and differences.

Mott Insulator

Inside the lobes the system behaves as an insulator. In the MI phase the minimum energy configuration is characterized by the same integer number n of bosons at each lattice site, i.e. integer filling condition. Notice, that in this case the total number of particles is $N = nM$, where M is the total number of wells. In this state the total number of bosons is fixed and a finite energy cost is required to add (subtract) a single boson to (from) any lattice site.

These features lead to two important consequences. Firstly, since the MI state is characterized by a frozen number of bosons per site, the compressibility, defined as

$$\kappa = \tfrac{\partial N}{\partial \mu},$$

vanishes. For this reason, the Mott insulator is said to be incompressible. Secondly, the energy cost to create (destroy) a particle leads to the opening of a gap in the excitations spectrum. For any point within a MI phase, the energy gap for particle (hole) excitations is simply the distance in the μ direction, with fixed J, from the upper (lower) boundary of the lobe, i.e. the minimum energy distance which allows extra particles (holes) to be added in the system.

In the Mott insulator phase, when the interactions dominate in the Hamiltonian (i.e. $J << U$), the ground state of the system consists of localized atomic wavefunctions with a fixed number of bosons per site. It follows, that the many-body ground state of the system is the product of local Fock states for each lattice site. In the case of filling factor n we have

$$|\Psi_{MI}\rangle_{J<<U} \propto \prod_{i=1}^{M} \left(\hat{a}_i^{\dagger}\right)^n |0\rangle \, . \tag{1.23}$$

where $|0\rangle$ is the single site state with zero bosons.

In general, for the MI state hold

1. $\langle \hat{n}_i \rangle = \langle \Psi_{MI} | \, \hat{n}_i \, | \Psi_{MI} \rangle = n \in \mathbb{N}$;
2. $\Delta n_i = \langle \hat{n}_i^2 \rangle - \langle \hat{n}_i \rangle^2 \to 0 \quad \text{for} \quad J/U \to 0$;

stating that, in the MI phase, quantum fluctuations vanish in the limit of small J/U. This result allows for the following remark. Let us introduce the local order parameter

$$\psi_i \equiv \langle \hat{a}_i \rangle = |\psi_i| e^{i\phi_i} \simeq \sqrt{n_i} e^{i\phi_i}, \tag{1.24}$$

where $\hat{\phi}_i$ is the phase operator that plays the role of canonical conjugate variable of $\hat{n}_i$, since it holds $\left[\hat{n}_i, \hat{\phi}_i\right] = i$. Due to the Heisenberg's uncertainty principle,

$$\Delta n_i \Delta \phi_i \geq \tfrac{\hbar}{2},$$

the absence of quantum fluctuations leads to the complete decoherence of the phase ϕ_i of the local order parameter describing the MI state ($\Delta\phi_i \to \infty$).

Superfluid

Outside the lobes the system is superfluid. In this phase the bosons are delocalized within the lattice and the creation or destruction of a particle has zero energy cost. In other words each site can have a different number of particles (i.e. no more integer filling) and the hopping is energetically favored. In this scenario the system is compressible, namely $\kappa \neq 0$, and gapless.

Deep in the SF phase, when the tunneling term dominates in the Hamiltonian (i.e. $J >> U$), the ground state energy is minimized if the single particle wavefunctions are spread out over the entire lattice. The many-body ground state is thus described by the macroscopic wavefunction

$$|\Psi_{SF}\rangle_{J>>U} \propto \left(\sum_{i=1}^{M} \hat{a}_i^\dagger \right)^N |0\rangle \,. \tag{1.25}$$

In general, for the SF state hold

1. $\langle \hat{n}_i \rangle = \langle \Psi_{SF} | \, \hat{n}_i \, | \Psi_{SF} \rangle$ can take any value;
2. $\Delta n_i = \langle \hat{n}_i^2 \rangle - \langle \hat{n}_i \rangle^2 \neq 0 \quad \forall \quad J/U.$

In other words, quantum fluctuations do not vanish for all values of the parameter J/U. This implies that in the superfluid regime the phase coherence is preserved and each site exhibits the same local order parameter phase ϕ_i.

The particular lobelike shape of the Mott insulator state in the zero-temperature phase diagram of the BH model can be qualitatively understood as follows [28]. Let us consider a point in the μ/U-J/U plane in the MI phase, then, by fixing the value of J, we will start to increase the value of the chemical potential. As μ grows, one will eventually find a point in the phase diagram where the kinetic energy gained by introducing a particle in the system which can hop around the lattice will balance the relative potential energy cost. As a consequence, the presence of a non zero number of quasiparticles free to move between the sites of the lattice at zero-temperature will lead to a Bose condensation letting the system move to the superfluid state. The same process occurs if, from our starting point in the MI phase, we fix J and we start decreasing the chemical potential. In this case, the kinetic energy gain is due removing a boson, that can be seen as the creation of a hole in the system. The latter, when are free to hop within the lattice sites at zero-temperature, they immediately Bose condensate letting the system reach a SF state. The two points we introduced in the above description are exactly the points of the phase diagram placed in correspondence of the lobes boundary. In figure 1.4 is reported the behavior of the density of boson n as a function of μ/U for a given value of the hopping amplitude.

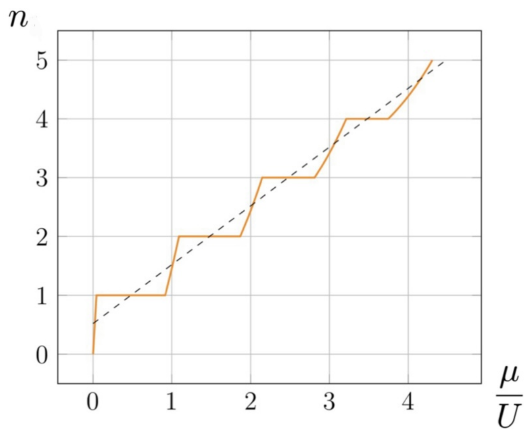

Figure 1.4: Behavior of the number of particles per site n as a function of μ/U for a fixed value of J at zero temperature. The regions in which n is constant correspond to the MI phase, i.e. coincide with the points of the phase diagram inside the lobes. In contrast, the regions in which the filling factor n grows with μ coincide with the SF phase.

Moreover, the fact that the kinetic energy of both particles and holes increases with J allows to understand that the width in μ of the MI state decreases by increasing J leading to the lobe shape reported in the phase diagram in figure 1.3.

The shape of the lobes in the phase diagram suggests for the presence of two different types of transitions [17, 28]: a *generic transition*, when the phase boundary is crossed at fixed J/U, and a *special transition* at fixed integer density when the lobe boundary is crossed at fixed μ/U. The *generic transition* is driven by the addition or the subtraction of a small number of particles, i.e. the same mechanism we previously described when we qualitatively explained the lobelike structure of the phase diagram. The *special transition*, that occurs at fixed integer density n at the tip of the lobes, instead is driven by a quite different physics. The density of particles never changes, but sufficiently large values of the hopping amplitude J enable the bosons to overcome the onsite repulsion and hop throughout the lattice, hence Bose condensing in the SF phase.

Finally, we conclude the chapter by reporting the mean field results for the phase diagram of the Bose-Hubbard model from Ref. [28]. The equation that relates the variables of the phase diagram reads

$$\frac{dJ}{U} = \frac{1}{2(\mu/U+1)}\left(\frac{\mu}{U} - (n-1)\right)\left(n - \frac{\mu}{U}\right), \tag{1.26}$$

where d is the spatial dimension of the system. From the latter equation, one is able to recover the expression for the lobes boundary $\mathcal{L}_n$, explicitly

$$\frac{\mu}{U} = n - \frac{1}{2} - \frac{dJ}{U} \pm \sqrt{\left(\frac{dJ}{U}\right)^2 - \frac{dJ}{U}(2n+1) + \frac{1}{4}}, \tag{1.27}$$

and the values of the critical parameters at the tip of the lobes

$$\begin{aligned}\left(\frac{\mu}{U}\right)_c &= -1 + \sqrt{n(n+1)},\\ d\left(\frac{J}{U}\right)_c &= \frac{1}{2} + n - \sqrt{n(n+1)}.\end{aligned}$$

Chapter 2

Worm Algorithm quantum Monte Carlo

As anticipated, the aim of the thesis is to study the low temperature behavior of a gas of dipolar bosons trapped in an optical lattice. In this regard, Monte Carlo simulations are exploited in order to capture the interesting properties of the many-body system. Before directly starting with the numerical analysis, is actually important to review the general ideas behind MC simulations and to introduce the algorithm that will play a prominent role in this dissertation: the worm algorithm quantum Monte Carlo.

This chapter will be thus structured as follows. We will start with a brief review of the Monte Carlo methods and of the Metropolis algorithm. We will then move on to the description of the path integral quantum Monte Carlo, a particular class of MC methods that plays a crucial role in the analysis of the Bose-Hubbard model at low temperatures. Finally, we will end the chapter with the description of the worm algorithm. We will understand its relation with PIMC and its contribution in the field of bosonic lattice systems.

2.1 Monte Carlo and Metropolis methods

Monte Carlo simulations are one of the most powerful numerical tool to study complex systems. Exploiting randomness through repeated random sampling, they allow to obtain numerical results for deterministic problems that cannot be treated analytically. For these reasons, this class of methods is widely used in various fields of science, engineering and mathematics.

In the first part of the chapter we will review some of the basic ideas behind MC methods applied to discrete classical systems, using as reference the notes by professor N. Prokof'ev [43].

Classical Monte Carlo

Let us suppose we need to evaluate the ratio of two N-dimensional sums of the form

$$\langle A\rangle = \frac{\sum_{i_1}\sum_{i_2}\cdots\sum_{i_N} A(i_1,i_2,\ldots,i_N)W(i_1,i_2,\ldots,i_N)}{Z}, \tag{2.1}$$

with

$$Z = \sum_{i_1}\sum_{i_2}\cdots\sum_{i_N} W(i_1,i_2,\ldots,i_N), \tag{2.2}$$

for arbitrary functions A and W. By introducing the notion of configuration ν, that is just the collection of all summation indices: $\nu = \{i_1, i_2, \ldots, i_N\}$ and by assuming W positive defined we can interpret the quantity

$$p(\nu) = \tfrac{W(\nu)}{Z}$$

as the probability of the configuration ν. In this regard, expression (2.1) may be considered as the average of the quantity $A(\nu)$ over all possible configurations where each configuration gives a contribution proportional to its weight $W(\nu)$. We can thus write

$$\langle A\rangle = \frac{\sum_\nu A(\nu)W(\nu)}{\sum_\nu W(\nu)} = \sum_\nu A(\nu)p(\nu). \tag{2.3}$$

A direct evaluation of these sums becomes impractical when N is large, since the number of configurations grows exponentially with N. Even with substantial computational resources, an explicit summation over all possible configurations is typically unfeasible. It is exactly for that type of problem that Monte Carlo simulations allow to compute in an efficient way the value of expression (2.1). The success of MC methods and the hope that the result of the calculation can be obtained in a reasonable time and with controlled accuracy are supported by the following two considerations.

First, the functions A and W typically take similar values for an important number of configurations, meaning that the configurations that are associated with the same values of the observable describe a large subset of the configuration space. In this regard, it is not necessary to investigate the contribution of each configuration, but it is sufficient to consider a large representative set that allows to capture the correct contribution coming from the different regions of the configuration space.

Second, in many physically relevant problems the weight function $W(\nu)$ presents a non-uniform behavior. Most configurations are characterized by a negligible weight, while only a small fraction contributes significantly to the evaluation of $\langle A\rangle$. It follows, that what is necessary in this case, is a clever procedure of summing up only the most important terms, neglecting the configurations with small weight. Consequently, an efficient strategy must be to select configurations according to their statistical relevance, since choosing configurations with uniform probability over the configuration space will lead with high probability to pick a configuration outside the relevant region.

These considerations evince the importance to add to the sum (2.1) configurations with probability proportional to their weight, in this way the likelihood to select a relevant configuration for the result is higher. A practical implementation of this strategy is provided by the well-known Metropolis algorithm.

Metropolis algorithm

The Metropolis algorithm is a Markov chain Monte Carlo method introduced for the first time by N. Metropolis *et al.* in 1953 to compute the equations of state for a generic substance composed of interacting individual molecules [44]. The algorithm was further studied and generalized by W. K. Hastings in his work published in 1970 [45] and, for this reason, the resulting method is typically known as the Metropolis Hastings algorithm.

The main idea behind MetA is to sum up only the most important terms in such a way to reproduce, with a good accuracy, the correct value of $\langle A \rangle$ without summing over all the configurations of the phase space. In this regard, Metropolis algorithm suggests to replace the original sum over all configurations with a stochastic sum of the form

$$\frac{\sum_\nu A(\nu)W(\nu)}{\sum_\nu W(\nu)} \quad \Longrightarrow \quad \frac{\sum'_\nu A(\nu)}{\sum'_\nu} \tag{2.4}$$

where configurations to be included into the sum $\sum'_\nu$ are generated using random numbers with probabilities proportional to their weights. It can be proved that in the limit of infinite calculation time the full sum (2.1) and the stochastic sum (2.4) will agree with each other exactly.

The MetA belongs to the class of Markov chain Monte Carlo method. A MCMC describes a class of algorithms that use Markov chains to generate a sequence of samples from a target probability distribution. These algorithms are able to build an ergodic chain characterized by the markovian property, i.e. each new sample exclusively depends on the previous one, and whose long term behavior reproduces a target distribution. Taking into account our previous discussion, the job done by a MCMC method exactly satisfies our goal. In fact, the possibility to extract configurations from the configuration space according to the distribution $p(\nu)$ allows us to introduce in the sum (2.4) configurations with large weight $W(\nu)$ that are the ones which mainly contributes to the calculation of $\langle A \rangle$.

In order to understand how Metropolis algorithm works, let us consider a particular case of the framework we have introduced before. We consider a discrete and conservative physical system at equilibrium (e.g. an Ising spin system). The problem we want to solve is the one of finding an efficient way to compute the average value of the physical observable A, namely

$$\langle A \rangle = \frac{1}{Z} \sum_{i=1}^{\mathcal{N}} A(c_i) e^{-\beta H(c_i)}, \tag{2.5}$$

where $Z = \sum_i \exp\left(-\beta H(c_i)\right)$ is the partition function of the system, β is the inverse temperature and H is the Hamiltonian. Firstly, one can notice that the latter expression is simply the application of equation (2.1) to the field of statistical mechanics. In fact, the quantities c_i describe the possible configurations of the systems with $i = 1, \dots, \mathcal{N}$ and $\mathcal{N}$ the total number of configurations. Moreover, in this context, the probability characterizing each configuration is given by the well known Boltzmann distribution

$$p_B(c_i) = \frac{W(c_i)}{Z} = \frac{e^{-\beta H(c_i)}}{Z} \qquad i = 1, \dots, \mathcal{N}. \tag{2.6}$$

The problematic aspects associated with the computation of (2.5) arise when the total number of configurations $\mathcal{N}$ is large. In this case, a direct computation of $\langle A \rangle$ is untreatable. However, as we have already highlighted, only a small fraction of configurations, and thus only a small region of the configuration space, actually contributes to the value of $\langle A \rangle$, while the rest of the configurations lead to a negligible contribution to the calculation. In this regard, the idea could be to compute expression (2.5) by not summing over all configurations, but to sum only an a reduced set of them in which every configuration is characterized by a large Boltzmann weight. Therefore, we simply need a method to select configurations based on their weight, i.e. we need to generate a sequence of samples whose behavior mimics the Boltzmann distribution. The latter could be accomplished by the Metropolis algorithm.

To reach the goal, MetA exploits the properties and the approach to equilibrium of the Markov chains. We recall that, the time evolution of a discrete-time Markov chain can be written as

$$\pi_j^{(t+1)} - \pi_j^{(t)} = \sum_{i \neq j} \left(P_{ij} \pi_i^{(t)} - P_{ji} \pi_j^{(t)} \right), \tag{2.7}$$

where $\pi_i^{(t)}$ is the probability to be in configuration c_i at time t and P_{ij} is the i, j-th element of the transition matrix $\mathcal{P}$, i.e. it is the value of the probability that the system performs a transition from state c_i to state c_j. At the steady state, equation (2.7) reaches its equilibrium version, namely the so called balance equation

$$\sum_{i \neq j} \left(P_{ij} \pi_i^{eq} - P_{ji} \pi_j^{eq} \right) = 0. \tag{2.8}$$

The latter equation has multiples solutions, but the simplest way to satisfy the balance equation is to balance updates in pairs, namely through the famous detailed balance condition, that reads

$$P_{ij} \pi_i^{eq} = P_{ji} \pi_j^{eq} \qquad \forall\, i, j = 1, \dots, \mathcal{N} \ \wedge \ i \neq j. \tag{2.9}$$

To relate the description in terms of Markov chain with our original problem, it is straightforward to choose as target equilibrium distribution of the chain the Boltzmann measure, namely

$$\pi_i^{eq} = p_B(c_i) = \tfrac{1}{Z} e^{-\beta H(c_i)} \qquad i = 1, \dots, \mathcal{N}.$$

We need now to find a correct expression for the transition matrix that allows to reproduce the Boltzmann distribution as the equilibrium distribution of the Markov chain. A possible choice for $\mathcal{P}$ that fulfill (2.9) and is numerically tractable could be

$$\begin{cases} P_{ij} = \pi_j^{eq}/\pi_i^{eq}, \quad P_{ji} = 1 & \text{if} \quad \pi_j^{eq} \le \pi_i^{eq} \\ P_{ij} = 1, \quad P_{ji} = \pi_i^{eq}/\pi_j^{eq} & \text{if} \quad \pi_j^{eq} > \pi_i^{eq}. \end{cases} \tag{2.10}$$

So far we have simply built a Markov chain that has the Boltzmann measure as the target equilibrium probability distribution. Then we now want to exploit this result to concretely construct a stochastic process that samples configurations according to the Boltzmann distribution. Explicitly

$$c^{(1)}, c^{(2)}, \dots, c^{(n)}, \dots \sim p_B,$$

where $c^{(n)}$ indicates the configurations of the system at the time step n. To do so, we divide each element of the transition matrix into the product of two contributions

$$P_{ij} = P_{ij}^{Tr} P_{ij}^{Acc}, \tag{2.11}$$

where:

- P_{ij}^{Tr} is the trial probability and describes the so called trial process, namely the process in which a new configuration is proposed;
- P_{ij}^{Acc} is the acceptance probability. It describes the condition over which a new configuration is accepted or rejected;

and, starting from a given initial configuration $c^{(n)} = c_i$ at time n, we proceed as follows:

1. Step 1: **choose a new configuration**

   a candidate configuration $c^T = c_j$ is selected with probability P_{ij}^{Tr}. In general, the new configuration is chosen using a trial probability such that $P_{ij}^{Tr} = P_{ji}^{Tr}$. In this way, the detailed balance condition reduces to

   $$\frac{P_{ij}}{P_{ji}} = \frac{P_{ij}^{Acc}}{P_{ji}^{Acc}} = \frac{\pi_j^{eq}}{\pi_i^{eq}} = \exp\left\{-\beta(H(c_j) - H(c_i))\right\} = \exp\left(-\beta \Delta H\right) \overset{(1)}{=} R,$$

   where in (1) we have defined the acceptance ratio R that can be simply computed starting from the energy difference of the trial configuration c_j and the original one c_i and, as we shall see, it represents a key quantity for the next step of the algorithm.

2. Step 2: **accept or reject the trial configuration**

   using the relation obtained at step 1 one can find a possible expression for the acceptance probability as a function of R. A possible solution reads

$$P_{ij}^{Acc} = \begin{cases} R & \text{if} \quad R \leq 1 \\ 1 & \text{if} \quad R > 1 \end{cases}$$

$$P_{ji}^{Acc} = \begin{cases} 1 & \text{if} \quad R \leq 1 \\ 1/R & \text{if} \quad R > 1. \end{cases}$$

   Once the acceptance probability is known, the algorithm decides to accept or reject the configuration c^T in the following way. It selects a random number r uniformly distributed between 0 and 1, then, if $r \leq P_{ij}^{Acc}$ it accepts the new configuration, i.e $c^{(n+1)} \to c^T$, otherwise it rejects the update, namely $c^{(n+1)} \to c^{(n)}$.

3. Step 3: **Go back to step 1 and cycle**.

The steps we have presented are exactly the ones that characterize the Metropolis algorithm. Following this procedure, we can, in fact, obtain a sequence of configurations that behaves according to the Boltzmann measure and thus allows one to select the most relevant contributions for the computation of $\langle A \rangle$.

In this section, we highlighted the importance of the Monte Carlo methods and of the Metropolis algorithm for the analysis of complex systems, and described how these approaches work. In the following, we will focus on a particular MC technique: the worm algorithm quantum Monte Carlo.

2.2 Path Integral quantum Monte Carlo and Worm Algorithm

Quantum Monte Carlo are considered one of the most powerful methods to study the equilibrium properties of strongly interacting many-body quantum systems. In fact, for such type of systems, the Hilbert space is extremely large and exact diagonalization methods cannot be applied.

There exist different MC techniques that can be used to analyze quantum systems. The one exploited in this work is the path integral quantum Monte Carlo implemented with the worm algorithm.

In this section, we will thus introduce PIMC, focusing on the case of bosonic lattice systems, and describe how the WA works.

2.2.1 Path Integral quantum Monte Carlo

PIMC is a method based on the path integral representation of quantum mechanics and on the so called imaginary time approach [22, 46]. In order to understand this idea, let us start by introducing the expression for the expectation value of an observable $\hat{O}$ according to quantum statistical mechanics, namely,

$$\left\langle \hat{O} \right\rangle = \mathrm{Tr}\left(\hat{\rho}\hat{O}\right), \tag{2.12}$$

where

$$\hat{\rho} = \frac{e^{-\beta\hat{H}}}{\mathrm{Tr}\left(e^{-\beta\hat{H}}\right)} = \frac{e^{-\beta\hat{H}}}{Z} \tag{2.13}$$

is the density matrix operator, β is the inverse temperature, $\hat{H}$ is the Hamiltonian operator of the systema and Z is the partition function.

We can now recall that the time evolution of an operator in the Heisenberg picture is given by the following equation

$$-i\hbar\frac{d\hat{O}}{dt} = \left[\hat{H}, \hat{O}\right], \tag{2.14}$$

whose general solution is

$$\hat{O} = \hat{U}^{\dagger}(t)\hat{O}\hat{U}(t), \tag{2.15}$$

where

$$\hat{U}(t) = \exp\left(-\frac{i}{\hbar}\hat{H}t\right) \tag{2.16}$$

is the time evolution operator.

By performing the change of variable $\beta = it/\hbar$, we can rewrite equation (2.14) in the so called imaginary time picture, namely

$$\frac{d\hat{O}}{d\beta} = \left[\hat{H}, \hat{O}\right], \tag{2.17}$$

whose general solution reads

$$\hat{O} = \hat{U}^{\dagger}(\beta)\hat{O}\hat{U}(\beta), \tag{2.18}$$

where

$$\hat{U}(\beta) = \exp\left(-\beta\hat{H}\right) \tag{2.19}$$

represents the imaginary-time evolution operator.

It is now evident that the density matrix operator (2.13) not only satisfies equations (2.17) and (2.18), but it is exactly proportional to the imaginary time evolution operator (2.19). This analogy is crucial since it allows to evaluate the expectation values of physical observables, and thus the partition function of the system, as an imaginary time evolution.

General principles

Now that we understand the idea of imaginary time evolution, we are ready to present the general principles behind PIMC and how the algorithm uses the previously mentioned concepts. To do so, we will follow the description reported in [17, 22, 46, 47], where the discussed imaginary-time scheme is developed starting from the interaction picture formalism. In this regard, let us consider a system described by the Hamiltonian $\hat{H} = \hat{H}_0 + \hat{H}_1$, where $\hat{H}_0$ is diagonal in some convenient basis set $\{|\alpha\rangle\}$, i.e. $\hat{H}_0 |\alpha\rangle = E_\alpha |\alpha\rangle$, while $\hat{H}_1$ is the off-diagonal part of the Hamiltonian. Within this context, we can express the imaginary-time evolution operator (2.19) as

$$e^{-\beta\hat{H}} = \hat{T}_\tau \Big[e^{-\int_0^\beta d\tau \left(\hat{H}_0 + \hat{H}_1(\tau)\right)} \Big] = e^{-\beta\hat{H}_0} \cdot \hat{T}_\tau \Big[e^{-\int_0^\beta d\tau \hat{H}_1(\tau)} \Big], \tag{2.20}$$

where $\hat{T}_\tau$ is the "time" ordering operator, τ is the imaginary-time variable and

$$\hat{H}_1(\tau) = e^{\hat{H}_0\tau} \hat{H}_1 e^{-\hat{H}_0\tau} \quad \text{with} \quad \hat{H}_1 = \hat{H}_1(\tau = 0)$$

is the non-diagonal part of the Hamiltonian expressed in the interaction representation.

Following the standard rules of many-body quantum field theory in the interaction picture, the Matsubara time evolution operator, defined as

$$\hat{\sigma} = \hat{T}_\tau \Big[e^{-\int_0^\beta d\tau \hat{H}_1(\tau)} \Big]$$

can be explicitly written as

$$\hat{\sigma} = \hat{T}_\tau \Big[e^{-\int_0^\beta d\tau \hat{H}_1(\tau)} \Big] = \mathbb{1} + \hat{\sigma}^{(1)} + \hat{\sigma}^{(2)} + \cdots + \hat{\sigma}^{(n)} + \dots, \tag{2.21}$$

where the generic, n-th order term, has the form

$$\hat{\sigma}^{(n)} = (-1)^n \int_0^\beta d\tau_n \cdots \int_0^{\tau_2} d\tau_1 \hat{H}_1(\tau_n) \hat{H}_1(\tau_{n-1}) \dots \hat{H}_1(\tau_1). \tag{2.22}$$

The chain of operators $\hat{H}_1(\tau_n)\hat{H}_1(\tau_{n-1}) \dots \hat{H}_1(\tau_1)$ describes the imaginary-time evolution of the system between the imaginary time $\tau = 0$ and $\tau = \beta$. Within this formalism the expectation value of a generic observable $\hat{O}$ can be written as

$$\langle O \rangle = \frac{1}{Z} \operatorname{Tr}\left(e^{-\beta\hat{H}} \hat{O} \right) = \frac{1}{Z} \sum_{\alpha,n} \langle \alpha | e^{-\beta\hat{H}_0} \hat{\sigma}^{(n)} \hat{O} | \alpha \rangle . \tag{2.23}$$

By explicitly writing $\hat{\sigma}^{(n)}$ in the latter expression, it is possible to obtain

$$\begin{aligned} \langle O \rangle &= \frac{1}{Z} \operatorname{Tr}\left(e^{-\beta\hat{H}} \hat{O} \right) \\ &= \frac{1}{Z} \sum_{\alpha,n} \int_0^\beta d\tau_n \cdots \int_0^{\tau_2} d\tau_1 (-1)^n e^{-\beta E_\alpha} \langle \alpha | \hat{H}_1(\tau_n) \hat{H}_1(\tau_{n-1}) \dots \hat{H}_1(\tau_1) |\Theta_\alpha\rangle , \end{aligned}$$

where $|\Theta_\alpha\rangle = \hat{O}\,|\alpha\rangle$ is the Fock state resulting from the action of the operator $\hat{O}$ on the state $|\alpha\rangle$. Notice that in case $\hat{O} = \mathbb{1}$ we recover the expression for the partition function of the system, namely

$$\begin{aligned} Z &= \mathrm{Tr}\left(e^{-\beta\hat{H}}\right) \\ &= \sum_{\alpha,n}\int_0^\beta d\tau_n \cdots \int_0^{\tau_2} d\tau_1 (-1)^n e^{-\beta E_\alpha} \langle\alpha|\,\hat{H}_1(\tau_n)\hat{H}_1(\tau_{n-1})\ldots\hat{H}_1(\tau_1)\,|\alpha\rangle\,. \end{aligned} \tag{2.24}$$

For this reason, in the following steps of the calculation we will consider the case $\hat{O} = \mathbb{1}$, since the same reasoning applies straightforwardly for the computation of the expectation value of a generic observable $\hat{O}$.

At this point, we introduce the completeness relation $\sum_{\alpha_i} |\alpha_i\rangle\langle\alpha_i|$ between every two consecutive operators $\hat{H}_1(\tau_i)$ in equation (2.24). In this way, it is possible to explicitly write the amplitude $\langle\alpha|\,\hat{H}_1(\tau_n)\hat{H}_1(\tau_{n-1})\ldots\hat{H}_1(\tau_1)\,|\alpha\rangle$ as a sum of amplitudes of all the possible paths from state $|\alpha\rangle$ to state $|\alpha\rangle$. Thus, we get

$$\begin{aligned} \langle\alpha|\,\hat{H}_1(\tau_n)\hat{H}_1(\tau_{n-1})\ldots\hat{H}_1(\tau_1)\,|\alpha\rangle = \sum_{\alpha_1,\ldots,\alpha_{n-1}} &\langle\alpha|\,\hat{H}_1(\tau_n)\,|\alpha_{n-1}\rangle \times \ldots \\ &\times \langle\alpha_i|\,\hat{H}_1(\tau_i)\,|\alpha_{i-1}\rangle \ldots \langle\alpha_1|\,\hat{H}_1(\tau_1)\,|\alpha\rangle\,. \end{aligned} \tag{2.25}$$

The amplitude of a single path is given by the product of all the intermediate transitional amplitudes describing the propagation from the intermediate state $|\alpha_{i-1}\rangle$ at time $\tau = \tau_{i-1}$ to the state $|\alpha_i\rangle$ at $\tau = \tau_i$. Expression (2.25) can be rewritten in a more compact form as

$$\begin{aligned} \langle\alpha|\,\hat{H}_1(\tau_n)\hat{H}_1(\tau_{n-1})\ldots\hat{H}_1(\tau_1)\,|\alpha\rangle = \sum_{\alpha_1,\ldots,\alpha_{n-1}} &H_1^{\alpha\alpha_{n-1}}(\tau_n) \times \ldots \\ &\times H_1^{\alpha_2\alpha_1}(\tau_2) H_1^{\alpha_1\alpha}(\tau_1), \end{aligned} \tag{2.26}$$

where the matrix elements $H_1^{\alpha_i\alpha_j}(\tau)$ reads

$$\begin{aligned} H_1^{\alpha_i\alpha_j}(\tau) &= \langle\alpha_i|\,\hat{H}_1(\tau)\,|\alpha_j\rangle \\ &= \langle\alpha_i|\,e^{\tau\hat{H}_0}\hat{H}_1 e^{-\tau\hat{H}_0}\,|\alpha_j\rangle = e^{\tau\left(E_{\alpha_i}-E_{\alpha_j}\right)}\langle\alpha_i|\,\hat{H}_1\,|\alpha_j\rangle\,. \end{aligned} \tag{2.27}$$

Now if we plug equations (2.26) and (2.27) in the expression (2.24) for the partition function, we recover a form of Z which contains off-diagonal matrix elements, $\langle\alpha_i|\,\hat{H}_1\,|\alpha_j\rangle$, and diagonals ones, E_{α_i}, in the exponents. This expression plays a fundamental role, since it provides the configuration space in which the PIMC algorithm makes updates.

Before continuing by specifying the Hamiltonian of the model, it is worth to highlight the following two aspects. First, in the current formalism, all the operators are gone and only scalars enter in the expression for the partition function. However, in doing so, we pay the price of introducing an extra dimension: the imaginary time dimension. Second, no approximation has been used.

PIMC and Bose-Hubbard model

Let us now specify the Hamiltonian of the system and try to analyze more in detail the configuration space. We consider the Bose-Hubbard model previously introduced, whose Hamiltonian reads

$$\hat{H} = -J \sum_{\langle i,j \rangle} \hat{a}_i^\dagger \hat{a}_j + \frac{U}{2} \sum_i \hat{n}_i(\hat{n}_i - 1) - \sum_i \mu_i \hat{n}_i, \tag{2.28}$$

and the Fock states $|\alpha\rangle = |n_1, \dots, n_i \dots, n_N\rangle$, where n_i is the occupation number of site i and N is the total number of sites of the system. Thus, it follows that, according to the notation we used before, the off-diagonal part $\hat{H}_1$ of the Hamiltonian coincides with the hopping term, while the remaining terms describe $\hat{H}_0$ since they are diagonal in the Fock basis.

Based on the Hamiltonian (2.28) the matrix elements (2.27) become

$$E_{\alpha_l} = \frac{U}{2} \sum_i n_i^{(\alpha_l)} \left(n_i^{(\alpha_l)} - 1 \right) - \sum_i \mu_i n_i^{(\alpha_l)} \tag{2.29}$$

and

$$\langle \alpha_l | \hat{H}_1 | \alpha_k \rangle = -J \sum_{\langle i,j \rangle} \langle \alpha_l | \hat{a}_i^\dagger \hat{a}_j | \alpha_k \rangle = -J \sqrt{\left(n_i^{(\alpha_k)} + 1 \right) n_j^{(\alpha_k)}}, \tag{2.30}$$

where $H_1^{\alpha_l \alpha_k}(\tau)$ is different from zero, if and only if the states $|\alpha_l\rangle$ and $|\alpha_k\rangle$ differ only in their occupation numbers at sites i and j such that $n_j^{(\alpha_l)} = n_j^{(\alpha_k)} - 1$ and $n_i^{(\alpha_l)} = n_i^{(\alpha_k)} + 1$.

At this point, exploiting equations (2.29) and (2.30), we are ready to write the expression of the partition function for the Bose-Hubbard model

$$Z = \sum_{n,\alpha} \sum_{\{\alpha_p\}} A_n \int_0^\beta d\tau_n \cdots \int_0^{\tau_2} d\tau_1 \exp\left\{ - \sum_{p=1}^{n} E_{\alpha_p} (\tau_p - \tau_{p-1}) \right\}, \tag{2.31}$$

where $\{\alpha_p\} = \alpha_1, \alpha_2, \dots, \alpha_{n-1}$ is the collection of the intermediate Fock states and A_n contains the product of square roots of hopping amplitudes of equations (2.30). Formally, expression (2.31) can be rewritten as

$$Z = \sum_{\{\nu\}} W_\nu, \tag{2.32}$$

where $\{\nu\}$ is a collection of discrete and continuous indexes labelling the configurations and W_ν is the weight of each configuration.

Let us now focus on the configurations over which the algorithm works. Each configuration represents a possible path of the system in imaginary time and can be pictorially depicted as in figure 2.1.

On the horizontal axis is present the imaginary time, while on the vertical axis are reported the sites of the lattice. Each line in the figure represents the

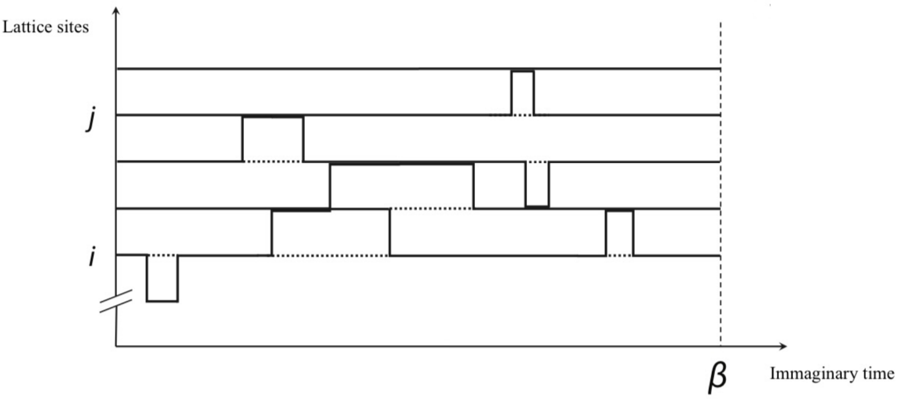

Figure 2.1: Example of a typical configuration in the CP space. On the horizontal axis is reported the imaginary time, while on the vertical one are present the lattice sites. Each world-line represents the imaginary-time evolution of a particle with "kinks" that describe the hop of the particle between nearest neighbors sites. The thickness of the line is proportional to the occupation number of the site at that particular imaginary-time instant. The figure is borrowed from [47].

imaginary-time evolution of a particle and is called world-line. The mathematical expression of the partition function as a trace entails that world-lines closed on themselves and that periodic boundary conditions in imaginary time have to be satisfied. By cutting the configuration at a certain imaginary-time instant τ_i, we obtain the system in a particular quantum state $|\alpha_i\rangle$. The points in imaginary time where a particle hops from one site to another, i.e. where the system changes state, are called "kinks". We call the phase space as "closed-path" (CP) configuration space [17]. The update procedure consists in changing the number of kinks of a given configuration and/or their position in imaginary time, but we will focus more in detail on updates in the next sections about WA.

2.2.2 Worm Algorithm

The Worm algorithm, originally developed by Prokof'ev *et al.* in [22], is a PIMC technique that works in an enlarged configuration space where a disconnected world-line, the worm, is allowed, see figure 2.2.

The configurations containing worms are generated by a generalized Hamiltonian of the form

$$\hat{H} \quad \rightarrow \quad \hat{H} - \gamma\hat{Q}, \tag{2.33}$$

where γ is an arbitrary coefficient that can be chosen in order to optimize the algorithm, while $\hat{Q}$ is the source term and owns an expression of the type

$$\hat{Q}(\tau) = \sum_i \left[\hat{a}_i^\dagger(\tau) + \hat{a}_i(\tau)\right], \tag{2.34}$$

where $\hat{a}_i(\tau) = \exp\left(\tau\hat{H}_0\right)\hat{a}_i \exp\left(-\tau\hat{H}_0\right)$ and $\hat{a}_i^\dagger(\tau) = \exp\left(\tau\hat{H}_0\right)\hat{a}_i^\dagger \exp\left(-\tau\hat{H}_0\right)$

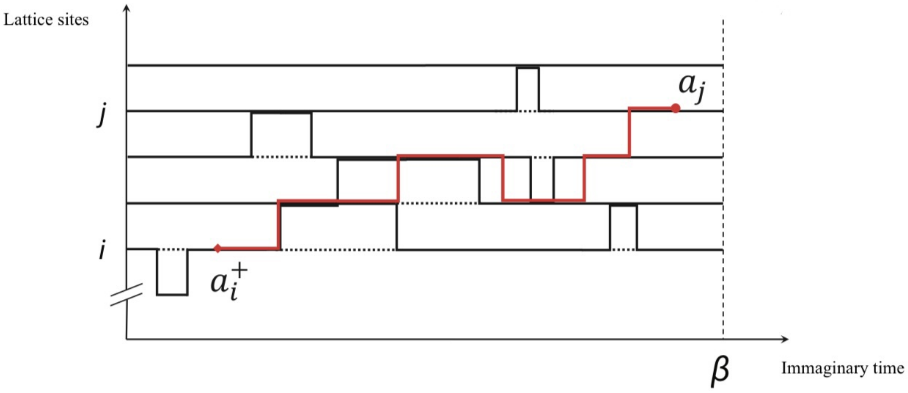

Figure 2.2: Example of a typical configuration in the CP_g space. The red disconnected world-line is called worm. The figure is borrowed from [47].

are, respectively, the annihilation and creation operator at site i expressed in the formalism of the interaction picture.

In the path integral formulation introduced before, the source term $\hat{Q}(\tau)$ is added to the off-diagonal term of the Hamiltonian $\hat{H}_1(\tau)$. In this way, by expanding the expression $\hat{T}_\tau\left[\exp\left(-\int_0^\beta \hat{H}_1(\tau)+\hat{Q}(\tau)d\tau\right)\right]$ we introduce terms with only one annihilation (creation) operator at different positions i (j) and time τ (τ'). These terms correspond to configurations with multiple disconnected world-lines, i.e. the worms, where the "head" and the "tail" of a worm correspond to the annihilation operator $a_j(\tau')$ and the creation operator $a_i^\dagger(\tau)$ respectively [47]. In our work only configurations with at most one worm are considered.

To sum up, there exist two different classes of configurations: those in which the worm is not present and those in which it is present. The first class of configurations, as we have seen, contributes to the statistics of the partition function Z and of physical observable $\hat{O}$. In contrast, the second class of configurations, since the operator $\hat{Q}(\tau)$ does not belong to the original Bose-Hubbard Hamiltonian, cannot be used to compute the expectation value of any physical observable. On the other hand, when the worm is present, configurations can be used to collect statistics for the Green function G. The latter, in the interaction picture formalism, is defined as

$$G(\mathbf{x}_i,\mathbf{x}_j,\tau,\tau')=\left\langle \hat{T}_\tau\left[\hat{a}_j(\tau')\hat{a}_i^\dagger(\tau)\right]\right\rangle . \tag{2.35}$$

For these reason we call the space of the configurations in which the worm is present as the CP_g space.

Let us now move on, exploiting the contents of [17, 22, 46, 47], to the update procedure. At each Monte Carlo step, a new configuration is proposed. All the update within the worm algorithm are local, i.e. they change the configuration on a local region in space and imaginary time. All updates but one are performed in the CP_g space, by moving the head or tail of a worm, as a sequence of drawing and erasing procedures. The only update performed in the CP space is the creation of a worm from a closed world-line. More in general, the updates of the algorithm can be divided into two categories: the updates that conserve the number of kinks and the ones that change the number of kinks. Let us try to describe more in detail these two classes of updates by the help of figures 2.3 and 2.4. In the pictures the bold dots describe the end point of a worm. The thickness of the world-line is associated with the occupation number, in particular, dotted lines contain n particles, normal lines contains $n + 1$ particles and the bold lines contain $n + 2$ particles. Moreover each world-line is divided into intervals in imaginary time, each of them delimited by kinks (depicted as crosses in the figures) and worm end.

In figure 2.3 a) and b) are reported the two updates that let the number of kinks unchanged. The first one, picture a), is the creation/destruction of a worm line. Describing the picture from left to right one can observe the creation of a worm, this particular update is in fact the only update that is performed in the CP space of configurations. A random interval of the configuration is selected, e.g. $\tau \in [\tau_{min}, \tau_{max}]$, and with the same probability one can draw (bottom panel) or erase (top panle) a segment of a world-line. In this way the chosen interval is now divided into three parts with the worm ends at imaginary times τ_1 and τ_2, where $\tau_{min} < \tau_1 < \tau_2 < \tau_{max}$. The opposite update, i.e. the destruction of a worm, is analogous and can be observed by reading the picture from right to left.

The second one, picture b), describe instead the shift of the worm end in imaginary time. As one can see from the figure the worm end is displaced forward in imaginary time (from left panel to the right one) or backward (from right panel to the left one).

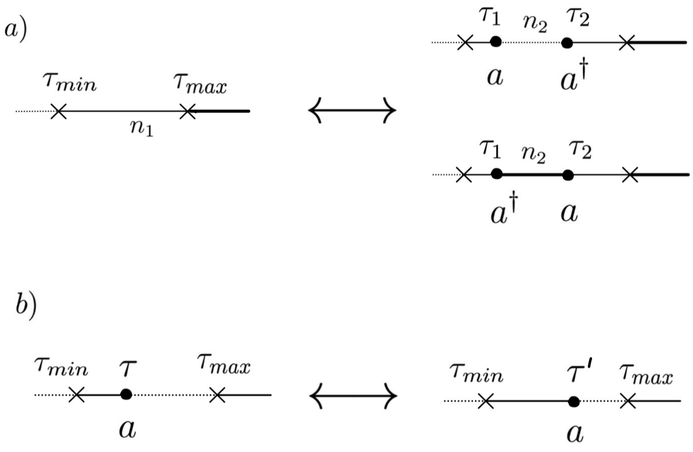

Figure 2.3: Graphical representation of the updates that conserve the number of kinks. In panel a) is presented the creation/destruction of a worm, while in b) is reported the shift in imaginary-time of a worm end. The figure is adapted from [17].

In figure 2.4 a) and b) are instead represented the updates that change the number of kinks in the configuration. The first one, i.e. picture a), describes the space shift left update, i.e. an update in which a kink is created or deleted by moving the end of the worm in space, on the left side of operator a (namely backward in time). The second one, i.e. picture b), describes the space shift right update, where, similar to case a), a kink is created or destroyed by moving the end of a worm in space, but in this case on the right side of the annihilation operator a (namely forward in time).

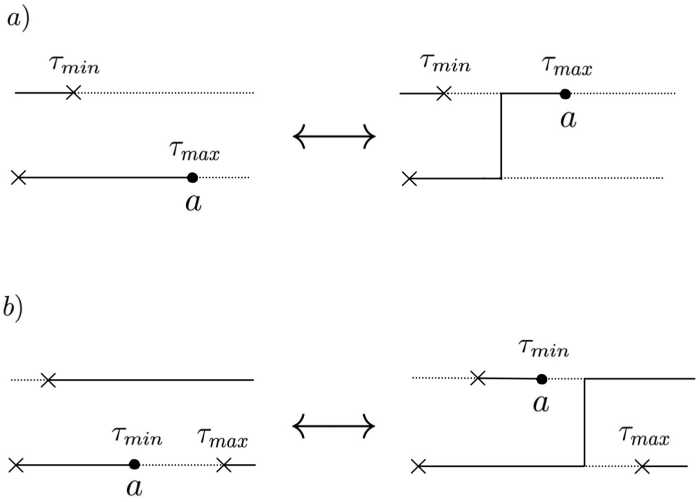

Figure 2.4: Graphical representation of the updates that change the number of kinks. In panel a) is presented the space shift left update, while in b) is reported the space shift right update. The figure is adapted from [17].

Let us end the section by underlying some of the most important benefits of the worm algorithm PIMC. Again our description is based on [17, 22, 46, 47].

Grand Canonical ensemble

The extension of the configuration space with the disconnected world-line allows us to work in the grand canonical ensemble with a number of particles that change during the steps of the algorithm. Moreover the chemical potential μ becomes a variable of the problem which allows us to determine the number of particles in the system.

Superfluid Density and Winding Numbers

Within the worm algorithm, it is possible to explore non-zero winding number configurations. The winding number $\mathcal{W}$ is an important parameter that describes how many times, in a given configuration, world-lines wind around the system in imaginary time. In order to clarify the concept, let us consider a one dimensional system with one particle, i.e. with a single world-line. Periodic boundary conditions in space and imaginary time are applied, leading the system to a torus. In figure 2.5 are reported two topologically different configurations of the system, where for simplicity we do not glue together the top faces of the cylinder. On the one hand, picture a) represents a configuration with zero winding number, since the world-line does not wind in imaginary time. On the other hand, picture b) represents a configuration with winding number equal to one, since the world-line winds once in imaginary time.

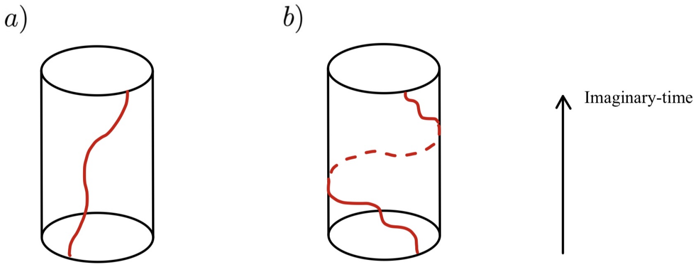

Figure 2.5: One dimensional system with a) winding number equal to zero; b) winding number equal to one.

The possibility to work with topologically different configurations is allowed by the fact that the update of the worm algorithm takes place in the CP_g space. In fact starting from a configuration with winding number $\mathcal{W}$ is always possible, by means of a sequence of local drawing and erasing steps, to reach a new configuration described by winding number $\mathcal{W}+1$ or $\mathcal{W}-1$. In contrast an algorithm that works only in the CP space would not be able to sample configuration with different winding numbers, since the only way to introduce a winding is to implement a global update that directly introduce a winding number. The problem is that the latter update is characterize by an extremely small acceptance ratio.

The possibility to perform statistics on the winding number during the steps of the algorithm is crucial since it allows to use these information to compute an important observable for studying the behavior of the systems: the superfluid density $\tilde{\rho}_s$. As reported in the paper [48] the superfluid density is related to the second moment of the winding number through the expression

$$\tilde{\rho}_s = \frac{mL^{2-d}}{\hbar^2 \beta d} \left\langle \boldsymbol{\mathcal{W}}^2 \right\rangle, \tag{2.36}$$

where $\beta = 1/k_B T$, L is the system size, d is the spatial dimension, m is the mass of the particles and $\boldsymbol{\mathcal{W}}^2 = \sum_{i=1}^{d} \mathcal{W}_i^2$.

In order to qualitatively understand why the superfluid density is related to the winding number and why it is important to characterize the superfluid phase of the system, we need to introduce the concept of gauge field [49]. In this regard let us consider a model strictly related to the BH one, i.e. the well known $|\psi|^4$ model, whose Hamiltonian reads

$$H = -\sum_{i,j} t_{i,j} \left[\psi_i^\star \psi_j + \psi_i \psi_j^\star\right] - c\sum_i |\psi|^2 + \frac{u}{2}\sum_i |\psi|^4, \tag{2.37}$$

where $\{\psi_i\}$ are complex valued variables. Lattice gauge field is defined by phase added to the hopping amplitude, namely

$$-\sum_{i,j} t_{i,j} \psi_i^\star \psi_j + c.c. \quad \rightarrow \quad -\sum_{i,j} t_{i,j} e^{i\phi_{i,j}} \psi_i^\star \psi_j + c.c.. \tag{2.38}$$

Exploiting the fact that ψ_i are complex variables, we can perform the substitution $\psi_i \to \psi_i e^{i\delta_i}$ and introduce in this way the gauge transformation from $\phi_{i,j}$ to $\tilde{\phi}_{i,j} = \phi_{i,j} + \delta_j - \delta_i$. Notice that, if by proper choices of the arbitrary phases δ_i we manage to make $\tilde{\phi}_{i,j}$ vanishing (or multiple of 2π) everywhere, than the model remains equivalent to the starting one.

Let us now consider, for example, a gauge field which has non-zero bond phase only along the $\hat{x}$-direction, namely

$$\phi_{i,\mu} = \delta_{\mu,\hat{x}} \frac{f_{i_x}}{L_x}, \tag{2.39}$$

where $\delta_{\mu,\hat{x}}$ is the Kronecker delta, f_{i_x} is an arbitrary function of the index i_x and L_x is the system size along the x direction. The notation we used is the same as the one reported in [49]: (i, μ) can be interpreted as a bond index, since $i = (i_x, i_y, \dots)$ is the site multi-index, while $\mu = 1, \dots, d$ describes the direction of the bond. For the next calculation let us only focus on what happen along the $\hat{x}$-direction, for simplicity we can thus consider a one dimensional lattice and set therefore $i = i_x$ and $\mu = \hat{x}$. Our aim is to find a proper choice of δ_{i_x} that makes all the gauge fields $\tilde{\phi}_{i_x,\hat{x}}$ disappear. A possible gauge transformation could be

$$\delta_{i_x} - \delta_{i_x-1} = -\tfrac{f_{i_x}}{L_x} \qquad \text{for} \quad i_x = 1, \dots, L_x.$$

Thanks to this choice we are able to make all the bond phases $\tilde{\phi}_{i_x,\hat{x}}$ become zero, except for $\tilde{\phi}_{L_x,\hat{x}}$ that reads

$$\tilde{\phi}_{L_x,\hat{x}} = \tfrac{\sum_{i_x=1}^{L_x} f_{i_x}}{L_x} =: \Phi.$$

The reason why we are not able to eliminate all bond phases by the gauge transformation performed on the ψ variables, is related to the fact that we are dealing with periodic boundary conditions, i.e. $\psi_{i+L_\mu\mu} \equiv \psi_i$. In other words we are imposing that sites obtained by going L_μ steps in the direction μ are identical to themselves. If instead we formally allow

$$\psi_{i+L_\mu\mu} = e^{-i\Phi}\psi_i, \tag{2.40}$$

then all gauge fields become equal to zero under gauge transformation. Equation (2.40) is known under the name of twisted boundary conditions, and is nothing but another way of looking at things which may be useful in some calculations. It is important to notice that in the case of twisted boundary conditions the variables ψ are single valued, and thus physically meaningful, only in the case in which Φ is a multiple of 2π. Nevertheless, even in the case in which $\Phi = 2n\pi$, and thus ψ_i takes the same value as $\psi_{i+L_\mu\mu}$, the order parameter is characterize by two different values of the phase, as if we are introducing n twists of the system in the μ-direction. As we will see this idea will play a crucial role in the analysis of the system since the phase of the variables ψ is an important observable for describing the behavior of the system.

We can now focus more in detail on the system response to this gauge field, or twisted boundary conditions. In this scenario the partition function and other thermodynamical quantities become functions of Φ. As proven in papers [49] and [50], in finite size systems the dependence on Φ is analytic, and for small Φ one may use Taylor series to write the free energy difference as

$$F(\Phi) - F(0) = \frac{\tilde{\rho}_s^{(x)} \Phi^2}{2m} \frac{V}{L_x^2}, \tag{2.41}$$

that in a more general case, namely the gauge field is non-zero in all directions $\mathbf{\Phi} = (\Phi_x, \Phi_y, \dots)$, it becomes

$$F(\Phi) - F(0) = \left(\frac{\tilde{\rho}_s}{2m} \right)_{\mu\nu} \frac{V \Phi_\mu \Phi_\nu}{L_\mu L_\nu}. \tag{2.42}$$

The latter equation can be actually considered as the definition of the superfluid density $\tilde{\rho}_s$, i.e. the linear response coefficient describing the free energy change in response to the gauge field. In other words, $\tilde{\rho}_s$ is the quantity that tells us which is the prize, in terms of free energy, that the system has to pay in order to introduce a phase twist equal to Φ between its end points.

From these last considerations is easy to understand why the superfluid density is related to superfluidity and how one can use this observable to study the possible phases of the system. In the superfluid phase the system is characterize by phase coherence of the order parameters ψ_i and therefore it is not favored to introduce a further phase factor Φ, that would destroy coherence. In this regard, the high free energy difference, $F(\Phi) - F(0)$, that one expects in the superfluid phase will lead to a finite value of $\tilde{\rho}_s$. In contrast, when we are dealing with a normal fluid, the introduction of Φ is not problematic for the system and thus the free energy that it has to pay would be very small leading to an almost vanishing value of the superfluid density.

For the sake of simplicity at the level of the algorithm, in the following we will work in terms of the so called superfluid stiffness. The superfluid stiffness, indicated with ρ_s, can be defined from the superfluid density in terms of the winding number through the relation

$$\rho_s = \frac{\tilde{\rho}_s}{m} = \frac{L^{2-d}}{\hbar^2 \beta d} \left\langle \boldsymbol{\mathcal{W}}^2 \right\rangle. \tag{2.43}$$

Since the two quantities simply differ by a multiplicative constant, the physical meaning of the superfluid stiffness is the same we just explained for the superfluid density.

Chapter 3

Extended Bose-Hubbard Model

In this chapter we will generalize the previous description about ultracold atoms trapped in optical lattices by introducing an extended version of the Bose-Hubbard model, the so called extended Bose-Hubbard model. The latter allows, in fact, to enrich the analysis of a bosonic system by incorporating a new class of interactions, such as long-range ones, in addition to the standard on-site interaction characterizing the BH model.

According to the purposes of this work, we will apply the EBH model to a system of dipolar bosons interacting through a long-range and anisotropic dipole-dipole interaction. Therefore, after a brief review of the dipolar interaction, we will introduce the concept of dipolar bosons and how one can model their behavior by means of the extended Bose-Hubbard model. We will end the chapter with a section dedicated to numerical simulations on dipolar bosons trapped in optical lattices, with special regard to quantum Monte Carlo techniques and worm algorithm.

3.1 The dipole-dipole Interaction

In order to study the physics of dipolar bosons in optical lattices, it is important to review the main features of the dipole-dipole interaction.

In this regard, using [51] as reference, let us consider two particles with dipole moments along the unit vectors $\mathbf{e}_1$ and $\mathbf{e}_2$ and relative position $\mathbf{r}$, as represented in figure 3.1. The energy due to the DDI between the particles reads

$$V_{dd}(\mathbf{r}) = \frac{C_{dd}}{4\pi} \frac{(\mathbf{e}_1 \cdot \mathbf{e}_2) r^2 - 3(\mathbf{e}_1 \cdot \mathbf{r})(\mathbf{e}_2 \cdot \mathbf{r})}{r^5}, \tag{3.1}$$

where C_{dd} is the coupling constant and is equal to $\mu_0 \mu^2$ for particles having a permanent magnetic dipole moment μ and d^2/ε_0 for particles having a permanent electric dipole moment d (μ_0 and ε_0 are respectively the permeability and permitivity of vacuum).

We can show that expression (3.1) can be simplified in the case of a polarized sample. In fact, when all dipoles point in the same direction, for instance z as in

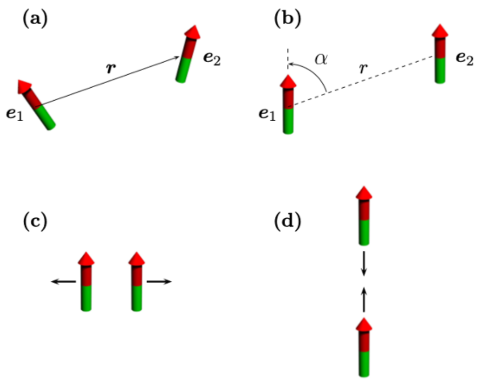

Figure 3.1: Two particles interacting through the dipole-dipole interaction. (a) Non-polarised case; (b) Polarised case (c) Side by side dipoles repel each others (d) 'Head-to-tail' particles attract each others. Figure adapted from [51].

panel (b) of figure 3.1, the DDI reduces to

$$V_{dd}(\mathbf{r}) = \frac{C_{dd}}{4\pi}\frac{1-3\cos^2(\alpha)}{r^3}, \tag{3.2}$$

where α is the angle between the direction of the polarization and the relative position of the particles.

By observing expression (3.2), we directly notice two important differences between the DDI and the well known isotropic and short-range van-der-Waals-like interaction. First at all dipole-dipole interaction is anisotropic. As α varies between 0 and 2π, the factor $1-3\cos^2(\alpha)$ varies between -2 and 1, and thus the DDI can be attractive (i.e. $V_{dd} < 0$) or repulsive (i.e. $V_{dd} > 0$) based on the value of the angle between the direction of the dipoles and the relative positions of the particles. In particular the DDI is repulsive for particles sitting side by side, while it is attractive for dipoles in a 'head-to-tail' configuration, as reported in panle (c) and (d) of figure 3.1. Secondly the DDI is long-range, since it scales as $1/r^n$ with $n = 3$.

3.2 Dipolar Bosons and Bose-Hubbard Model

In physics, particles that obey to the Bose-Einstein statistics and are thus characterized by integer values of spin are called bosons. Moreover, when bosonic particles own a permanent dipolar moment, either electric or magnetic, they are classified as dipolar bosons.

Because of recent experimental successes in obtaining Bose-Einstein condensates of atoms having large dipolar moments, such as ^{52}Cr [12, 52] and ^{164}Dy [13], systems composed by dipolar bosons become very popular and many studies on their behavior are developed.

A gas of ultracold dipolar bosons confined in an optical lattice exhibits a richer physics with respect to that of a gas of standard bosonic particles. In fact, because of the presence of a permanent dipole moment, dipolar bosons do not only interact through a short-range, on-site, repulsive interaction, that arises from the presence of two, or more, particles in the same lattice well, but they also interact through a long-range and anisotropic dipolar interaction that involves particles belonging to different sites of the optical lattice. It follows, that in this more complex scenario, the standard Bose-Hubbard model we have introduced in chapter 1 is not enough to capture the behavior of a system of interacting dipolar lattice bosons. To better understand the last idea, let us go back to some concepts about the BH model studied in the previous chapters.

We recall that the BH model is described by an Hamiltonian of the form

$$\hat{H}_{BH} = -J\sum_{\langle i,j\rangle} \hat{a}_i^\dagger \hat{a}_j + \frac{U}{2}\sum_i \hat{n}_i(\hat{n}_i - 1) + \sum_i \mu_i \hat{n}_i, \tag{3.3}$$

where J is the hopping amplitude, U is the strength of the local on-site interaction and $\mu_i = \mu - \varepsilon_i$ is the local chemical potential at site i. As mentioned, the Bose-Hubbard model has been widely studied in the last thirty years owing to the considerable interest raised by the well known SF-MI phase transition characterizing the system at zero temperature. The competition between the kinetic energy term, related to the hopping phenomenon, and the repulsive on-site interaction makes the system undergoes a quantum phase transition in which the ground state changes macroscopically its properties based on the value of the parameters entering in the Hamiltonian (3.3).

However, the Hamiltonian of the BH model highlights a limitation of the latter. In fact, despite its reputation, the Bose-Hubbard model is able to capture only the properties of bosonic systems characterized exclusively by on-site interaction, while it is not capable to describe the physics of those systems in which particles belonging from different lattice sites can interact through a generic long-range interaction. In this regard, in order to increase the set of systems that can be modeled by the BH model a generalization of the latter must be introduced. The generalized version of the Bose-Hubbard model is known as extended Bose-Hubbard model.

The extended Bose-Hubbard model is a theoretical framework in condensed matter physics which allows to enrich the analysis of a system of interacting bosons trapped in an optical lattice by including a new class of interactions, such as long-range ones, to the usual on-site interaction that describes the standard Bose-Hubbard model. The Hamiltonian of the EBH model can be written as

$$\begin{aligned}\hat{H}_{EBH} &= \hat{H}_{BH} + \frac{1}{2}\sum_{i\neq j} V_{ij}\hat{n}_i\hat{n}_j \\ &= -J\sum_{\langle i,j\rangle} \hat{a}_i^\dagger \hat{a}_j + \frac{U}{2}\sum_i \hat{n}_i(\hat{n}_i - 1) + \sum_i \mu_i \hat{n}_i + \frac{1}{2}\sum_{i\neq j} V_{ij}\hat{n}_i\hat{n}_j. \end{aligned} \tag{3.4}$$

The last term of the Hamiltonian, proportional to the product of the number operators $\hat{n}_i\hat{n}_j$, accounts for the long-range interaction between two particles occupying site i and site j of the lattice and V_{ij} is the coefficient characterizing the strength of that interaction. In the case of a gas of dipolar bosons, in which all dipoles point in the same direction, the coefficient V_{ij} takes the expression (3.2) giving an Hamiltonian of the form

$$\begin{aligned}\hat{H}_{EBH} = &- J\sum_{\langle i,j\rangle} \hat{a}_i^\dagger \hat{a}_j + \frac{U}{2}\sum_i \hat{n}_i(\hat{n}_i - 1) + \sum_i \mu_i \hat{n}_i + \\ &+ \frac{1}{2}\sum_{i\neq j} \frac{C_{dd}}{4\pi}\frac{1-\cos^2(\alpha)}{r_{ij}^3}\hat{n}_i\hat{n}_j, \end{aligned} \tag{3.5}$$

where r_{ij} is the magnitude of the vector describing the relative position between site i and site j and α is the angle between the direction of the dipole moments and the relative position of particles.

The increased complexity of the Hamiltonian (3.4), due to the presence of a long-range interaction, ensures that the EBH model will present a richer ground state phase diagram with respect to the one characterizing the standard BH model studied in chapter 1. In addition to Mott-insulating and superfluid states, new phases can be observed because of the competition between the coefficient V_{ij} and the other parameters entering in the Hamiltonian of the model. Specifically, the richer zero temperature phase diagram of the extended Bose-Hubbard model can include also the following phases: (i) density wave, an insulating state characterized by spatial modulation of the particles density, (ii) supersolid, a phase that presents the properties of both solids and superfluids, namely a phase in which both the diagonal crystalline order and off-diagonal superfluid long-range order coexist [53, 54] and (iii) Haldane insulator, a particular type of insulating phase with topological properties that can be observed in one-dimensional EBH models [55].

3.3 Brief overview of numerical results by the Worm Algorithm

Physical properties of ultracold dipolar bosons modeled by the extended Bose-Hubbard model have been widely studied over the years using both analytical and numerical methods. However, the complexity of these systems makes numerical simulations as the most convenient and exploited technique for their analysis. A class of methods that plays a crucial role in this research field is the one of quantum Monte Carlo. There exist multiple quantum MC techniques, such as variational Monte Carlo, diffusion Monte Carlo, auxiliary field Monte Carlo, etc, but one of the most suitable approaches for the analysis of ultracold gases of bosonic particles trapped in optical lattices is the worm algorithm, a special case of the more general

PIMC that we introduced in chapter 2. In fact, as we discussed in the previous chapters, the WA presents many benefits that are essential in this scenario. First at all, it allows to work in the grand canonical ensemble, and thus to make simulations varying the total number of particles in the system. Secondly, it is able to analyze configurations described by a non-zero winding number, leading to the possibility to compute important physical observables, such as the superfluid density, by simply exploiting the statistics of the winding number. Finally, it does not need to include any approximations, meaning that an exact description of the system can be done, at least, of course, of the intrinsic error that characterizes MC methods. Thanks to path integral Monte Carlo by the worm algorithm interesting results about the behavior of dipolar bosons have been obtained over the last thirty years. In the following we will report some examples.

In [56] the worm algorithm has been used to study the zero temperature phase diagram of a system of soft-core dipolar bosons confined in a two-dimensional optical lattice. The term soft-core bosons refers to bosonic systems in which there is the possibility of having more than one particle per lattice site at the same time, i.e. a scenario that can be formally described by the condition $U < \infty$. The authors of the paper assumed that electric dipoles are aligned perpendicular to the plane of the lattice, letting the dipole-dipole interaction become purely repulsive and isotropic. In this context they were able to observe quantum phases such as supersolid and checkerboard solid, namely, a particular density wave state in which bosons occupy the lattice sites in an alternating pattern, and also to study their stability against thermal fluctuations.

In works [57] and [58] was instead considered a system of hard-core dipolar bosons trapped in a two-dimensional lattice, where the term hard-core describes systems in which each potential well can contain at most one particles, i.e. it refers to the regime $U \to \infty$ where the bosonic creation operator fulfill the relation $\left(\hat{a}_i^\dagger\right)^2 = 0$ for all the sites i of the lattice. More in detail, in both works the dipoles are tilted and aligned by an external electric field, but, in [58] it was investigated the scenario in which the angle α between the relative direction of the particles and the direction of the dipoles is fixed to $90°$, while in [57] the angle α is not fixed and it is instead used as a parameter for the description of the phase diagram in order to capture how the system behaves after a variation of α. Both descriptions allow to explore important features of the system.

On the one hand in [58], the phase diagram is plotted in terms of chemical potential and hopping amplitude. In the limit of small tunneling, the authors found evidence for a devil's staircase, where Mott-solids appear at rational fillings of the lattice, while increasing the hopping amplitude they established the existence of extended regions of parameters where the ground state is supersolid.

On the other hand, in paper [57] the phase diagram is plotted in the $V_{dd} - \theta$ plane at half filling, where V_{dd} is the strength of the dipolar interaction and θ is the complementary angle of α. One can observe that for small values of V_{dd} the system behaves as a superfluid for almost all values of α, while for larger values of the strength of the dipole-dipole interaction the system is in a checkerboard state for small θ and in a solid stripe phase for large values of the same angle.

Paper [59] starts from a similar scenario as the one presented in paper [58], but it complicates the analysis by introducing also the presence of a random diagonal disorder. As one can imagine, the presence of disorder enriches the behavior of the system and a new exotic phase can be observed: the Bose glass. The Bose glass is a gapless phase characterized by a finite compressibility. It can be thought of as a Mott insulator containing rare islands of superfluid. These SF regions are not interconnected, making the system behave as an insulator. However, their presence significantly changes the thermodynamics properties of the system.

To conclude the qualitative analysis of how the WA can be used to study a system of dipolar lattice bosons, we focus on papers [60] and [61]. Both works study the ground state phase diagram of a gas of hard-core dipolar bosons trapped in a square lattice bilayer geometry, where not only particles interact in the same layer but also from a layer to the other. In [60] the two layers are aligned, while in [61] the authors worked with a twisted bilayer geometry in which the direction of the upper layer form an angle θ with the direction of the lower one. In this way they could understand how the twist of the layers affect the physical properties of the system. The aim of the works was to discuss the many-body effects resulting from the pairing of particles across two different layers. The latter leads, for instance, in the creation of a pair supersolid and a pair superfluid phases.

It is important to stress that, as we mentioned before, the PIMC and WA are important techniques to study ultracold bosons trapped in optical lattices. It follows, that these methods are not only used to analyze systems of dipolar bosons, but also other systems can be considered. An example is given by bosonic mixtures.

In paper [62] is presented a numerical work on a Bose-Bose mixture trapped in a two-dimensional lattice. In the latter is analyzed how the famous MI-SF transition of the majority component of the mixture is affected by the presence of a second species. The authors show how the boundary of the lobes in the phase diagram get renormalized by a variation of the concentration of the minority bosonic species and of the strength of its interaction with the majority one.

Another example of how the worm algorithm can be used to study ultracold mixtures is reported in [63]. In this paper, it is presented the ground state phase diagram of a system composed by a mixture of two bosonic species. Depending on the interplay between intra- and inter-species interactions, and on the filling condition of the lattice, different quantum phases are stabilized. More in detail, it has been shown that the ground state phase diagram at half filling feature demixing effects, i.e. the spatial separation of the two species of the mixture, when the inter-species interaction is larger than the intra-species repulsion. In these conditions, phases such as demixed superfluid and demixed Mott-insulator become stable. In contrast, when the inter-species interaction decreases and becomes lower than the intra-species repulsion the phase diagram is characterized by a double superfluid phase and a supercounterflow, namely an interesting state in which the two components of the mixture create two separate flows in opposite directions leading in this way to an insulating state with vanishing total current.

We conclude the chapter with a detailed analysis of a further work about the behavior of ultracold bosons trapped in optical lattices: *Quantum Phases and Instabilities in Anisotropic Dipolar Lattice Bosons* by Yaghmorassene Hebib, Chao Zhang and Barbara Capogrosso-Sansone [1]. The latter plays a crucial role in this thesis, since it represents the starting point for the main section of the dissertation.

In this manuscript, the authors explore the zero temperature phase diagram of a system of hard-core dipolar bosons at half filling situated in a two-dimensional square optical lattice. All the dipoles are aligned parallel to each others and tilted out of the lattice plane using an external electric field.

I. Introduction

The paper was strongly motivated by the findings of [2]. In [2], the extended Bose-Hubbard model has been realized by trapping magnetic erbium (Er) atoms in an optical square lattice. The experiment is conducted at half filling, and the tilt angle of the magnetic dipole moments is controlled via an external magnetic field, allowing for the exploration of a variety of tilt angles. Through the well-established quantum gas microscope technique, combined with the use of an accordion lattice, the authors of [2] were able to observe the position of single atoms on a 10×10 lattice at the center of the harmonic trap. They report on the experimental observation of dipolar solids, such as checkerboard and stripe quantum solids.

In this regard, Y. Hebib, C. Zhang and B. Capogrosso-Sansone in their manuscript investigate the zero temperature quantum phases of a system at half filling using path integral QMC by the worm algorithm, in order to compare their numerical results with the ones obtained experimentally with Er atoms in [2].

II. Hamiltonian

The choice to study hard-core particles aligns with the experimental realization [2] for which the on-site repulsion is much larger than all energy scales. In this scenario the dipoles are oriented parallel to each other along the direction of polarization, each with an induced dipole moment d. The direction of the polarization, which can be experimentally controlled with an external field, lies on a plane perpendicular to the optical lattice plane and at an angle of 45° with the x direction. In other words, considering a description in terms of spherical coordinates, they assume a fixed azimuthal angle $\phi = 45^\circ$ and vary the polar angle θ, as reported schematically in figure 3.2.

It follows, that the second quantization Hamiltonian describing the system is

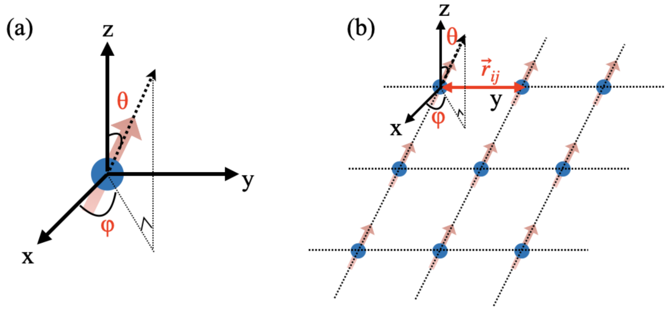

Figure 3.2: Schematic representation of the system. Dipoles are trapped in a two-dimensional optical lattice and are aligned parallel to each other along the direction of polarization. θ is the polar angle between polarization axis and the z direction, ϕ is the azimuthal angle (fix to 45° in this work) and $\mathbf{r}_{ij} = (x_{ij}, y_{ij})$ is the relative position between site i and site j. The figure is borrowed form [1].

exactly the one we reported in equation (3.5), namely

$$\hat{H} = -J\sum_{\langle i,j\rangle}\hat{a}_i^\dagger\hat{a}_j - \sum_i \mu_i\hat{n}_i + V\sum_{i<j}\frac{r_{ij}^2 - 3\sin^2\theta(x_{ij}\cos\phi + y_{ij}\sin\phi)^2}{r_{ij}^5}\hat{n}_i\hat{n}_j, \quad (3.6)$$

where the authors have simply re-express the dipole-dipole interaction in spherical coordinates, have defined $V = C_{dd}/4\pi$ and have removed the on-site interaction term since the particles are classified as hard-core.

In (3.6) $\hat{a}_i^\dagger$ ($\hat{a}_i$) are the bosonic creation (annihilation) operators with the usual commutation relations and satisfying the hard-core condition $\left(\hat{a}_i^\dagger\right)^2 = 0$, and $\hat{n}_i = \hat{a}_i^\dagger\hat{a}_i$ is the number operator associated to the i-th well of the lattice. The symbol $\langle \ldots \rangle$ is used to denote nearest neighbors sites. The first term in the Hamiltonian (3.6) describes the kinetic energy of the system with hopping energy J, the latter coefficient is used as unit of energy in the work. The second term $\mu_i = \mu - W_i$ is the sum of the chemical potential μ which sets the total number of particles and the confining potential W_i. The third term is the dipole-dipole interaction with V that is the coefficient describing the strength of the nearest neighbors repulsive interaction energy originated when all dipoles are oriented perpendicular to the lattice, $r_{ij} = |\mathbf{r_i} - \mathbf{r_j}| = |(x_{ij}, y_{ij})|$ is the relative distance between site i and site j, θ and ϕ are the polar and azimuthal angle, respectively (see figure 3.2).

In the following we report results at half filling, for $\phi = 45°$, $W_i = 0$ and periodic boundary conditions in space. A cut off equal to the system size (L) is applied to the dipolar interaction.

III. Phase diagram at $T = 0$

The zero temperature phase diagram of the system associated to the Hamiltonian (3.6), obtained with quantum MC simulations, is presented in the θ-V/J plane and is reported in figure 3.3.

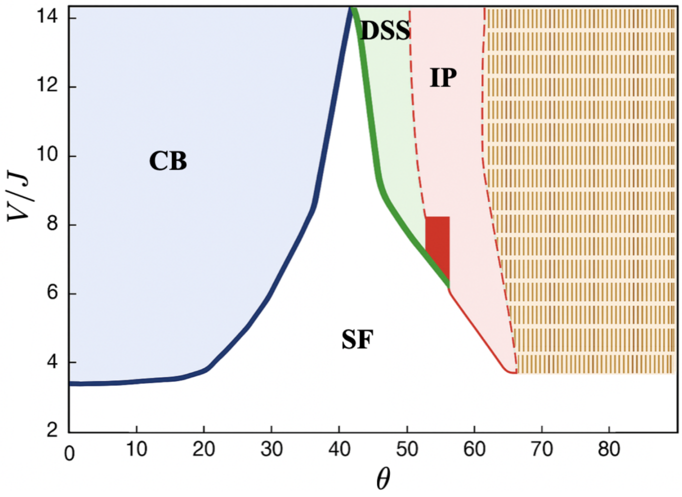

Figure 3.3: Zero temperature phase diagram of the system described by the equation (3.6) as a function of polar angle θ and V/J, at fixed azimuthal angle $\phi = 45°$. The harmonic confinement is absent. The system features a superfluid phase (SF), white region; a checkerboard solid (CB), blue region; a diagonal stripe solid (DSS), green region; an incompressible phase (IP), where particles arrange in diagonal stripes of various thickness separated by empty stripes also of various thickness, red region; and a phase separation (PS), in a small range of angles close to the right boundary of the red region. The brown dashed area is a region of instability for any densities $n \neq 0, 1$. In this region of parameter space the system is either empty ($n = 0$) or full ($n = 1$) undergoing a first order phase transition from empty to full as a function of the chemical potential μ at fixed V/J and θ. The figure is borrowed form [1].

For their simulations the authors considered system sizes within the range $6 \leq L \leq 48$ and an inverse temperature $\beta = L/J$ to ensure that the system is effectively at zero temperature. As customary in this field, all the results are reported in units of k_B, $\hbar$ and lattice step a.

The complexity of the model under analysis ensure a rich phase diagram in which four different phases are observed: superfluid, checkerboard solid, diagonal stripe solid and incompressible phases.

At lower interaction strengths V/J , the system remains in a SF phase regardless of the tilt angle θ. This phase is characterized by off-diagonal long-range order and finite superfluid stiffness ρ_s and compressibility κ. When the strength of the dipole dipole interaction is increased, the SF phase is destroyed in favor of dipolar solid phases, such as CB solid and DSS. In these solid phases, long-range diagonal order is indicated by a finite value of the structure factor S, that reads

$$S(\mathbf{k}) = \frac{1}{N} \sum_{\mathbf{r}.\mathbf{r}'} \exp(i\mathbf{k} \cdot (\mathbf{r} - \mathbf{r}')) \langle \hat{n}_{\mathbf{r}} \hat{n}_{\mathbf{r}'} \rangle \,, \tag{3.7}$$

where $\mathbf{k}$ is the reciprocal lattice vector. The structure factor is formally the Fourier transform of the density-density correlation. S exhibits peaks at positions set by the periodicity of the quantum solid state. For example, in the CB one has $\mathbf{k} = (\pi, \pi)$ while for DSS the peaks coincide with $\mathbf{k} = (\pi/2, \pi/2)$. Moreover, solid phases are incompressible, i.e. they are characterized by a compressibility $\kappa = 0$.

More precisely, as one can see in figure 3.3, for $\theta \lesssim 42^\circ$ there exists a θ-dependent V/J value at which the SF phase disappears in favor of a CB via a first order phase transition. As expected, the SF-CB transition boundary moves toward larger values of V/J for larger polar angles. This behavior is intuitive since, as the polar angle increases at fixed V/J, the repulsive nearest neighbors dipolar interaction decreases in favor of an increasing attractive interaction along the diagonal. For larger polar angles, instead, the superfluid phase becomes unstable in favor of a double-DSS before and a triple- and quadruple-DSS after. The latter describe diagonal solids with diagonal stripes whose thickness is two, three, or four sites respectively. The transition from SF to double-DSS is first order as well. The authors also note that, up to $V/J \sim 14$, the superfluid phase remains stable for a certain range of θ around $\theta \sim 42^\circ$, and intervenes between the CB and the DSS. This interesting finding results from the competition between repulsive interaction between nearest neighbors and attractive interaction along the diagonal that occurs at these intermediate angles. Moreover, when the strength of the dipolar interaction becomes large enough, i.e. $V/J > 14$, the SF phase no longer exists and a first order phase transition between CB and double-DSS is observed at $\theta \sim 42^\circ$.

As the polar angle increased, the system moves to a so called incompressible region, depicted in red in the phase diagram. The incompressible phase is characterized by the impossibility to observe a single solid order for a given pair of parameters $(\theta, V/J)$. For this range of parameters, depending on the system size and on the initial conditions, particles arrange in diagonal stripes of various thickness separated by empty stripes also of various thickness. The large the polar angle, the thicker the diagonal stripes can be observed. These findings suggest that in this region of the phase diagram there exist many local minima of the free energy of comparable value. Moreover, close to the right boundary of the IP, is observed a small range of polar angles for which the authors show the presence of phase separation between a region of unit filled sites and empty sites. To sum up, in picture 3.4 are reported some examples of density maps for the various phases encountered so far. Each circle corresponds to a different site of the lattice and its radius is proportional to the local density of particles at that site.

Finally, the brown dashed region in the phase diagram describes an instability region. For large values of the polar angle, i.e. $\theta \gtrsim 62^\circ$, the authors observe that half filling is no more stable. In other words, in this region, depending on the value of the chemical potential, the filling factor is either zero or one and a first order phase transition between empty and fully filled lattice is observed as a function of

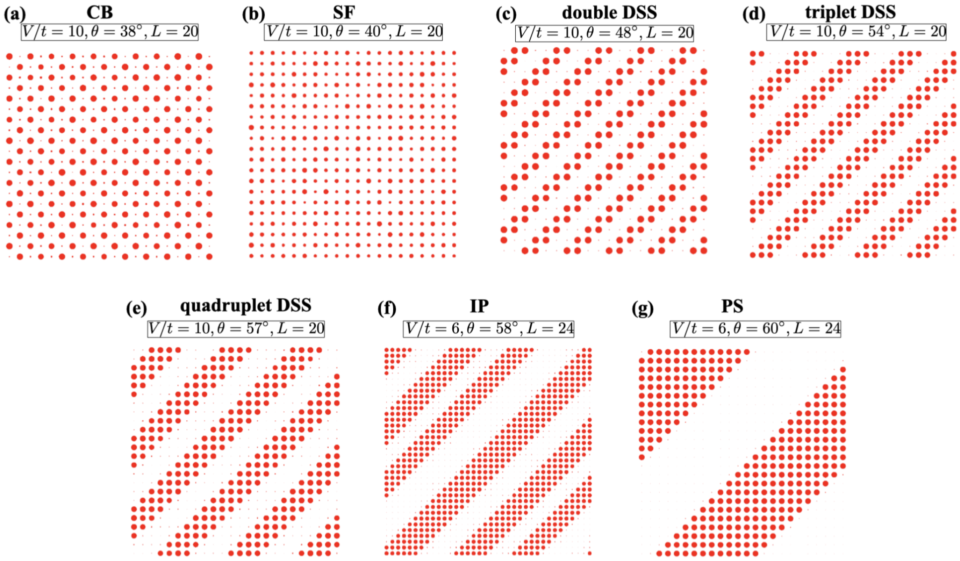

Figure 3.4: Density maps for various phases. Each circle corresponds to a different site of the lattice and its radius is proportional to the local density of particles at that site. For all panels, the parameters used and the type of phase obtained are reported on top of each plot. The figure is borrowed form [1].

the chemical potential.

The instability region obtained by Y. Hebib, C. Zhang and B. Capogrosso-Sansone using quantum Monte Carlo techniques represents an interesting result since it does not match the experimental findings obtained in [2] for large polar angles. In fact, if on the one hand the two papers agreed for what concern the quantum phases characterizing the system for small θ, on the other hand the results find for large polar angles do not coincide.

In the experiments conducted in [2], it has been shown that the system forms a diagonal solid in the region of the parameter space for which Y. Hebib, C. Zhang and B. Capogrosso-Sansone have found that half filling is unstable for the homogeneous system. Moreover, in [2], for angles $\theta \gtrsim 75°$, a self-bound insulator, i.e. a global phase separation state with the lattice separated into unity-filled and empty region, is observed. In contrast, in the work by Y. Hebib, C. Zhang and B. Capogrosso-Sansone was proven that such phase cannot be stabilized in the homogeneous system a part from a small range of polar angles close to the right boundary of the incompressible phase, i.e. $\theta \sim 60°$.

Chapter 4

Numerical Simulations and Results

This dissertation aims to study the finite temperature behavior of a system of hard-core dipolar bosons confined in a two-dimensional optical square lattice by means of a numerical approach involving quantum Monte Carlo simulations based on the worm algorithm [22].

The starting point of our work are the results reported in the draft paper [1]. The authors of [1] analyzed a two-dimensional system of lattice dipolar bosons modeled by the Hamiltonian of the extended Bose-Hubbard model that reads

$$\begin{aligned}\hat{H}_{DLB} = &- J\sum_{\langle i,j\rangle} \hat{a}_i^\dagger \hat{a}_j - \sum_i \mu_i \hat{n}_i + \\ &+ V\sum_{i<j} \frac{r_{ij}^2 - 3\sin^2\theta (x_{ij}\cos\phi + y_{ij}\sin\phi)^2}{r_{ij}^5} \hat{n}_i \hat{n}_j. \end{aligned} \tag{4.1}$$

Here, $\hat{a}_i^\dagger$ ($\hat{a}_i$) are the bosonic creation (annihilation) operators with the usual commutation relations and satisfying the hard-core condition $\hat{a}_i^{\dagger 2} = 0$, and $\hat{n}_i = \hat{a}_i^\dagger \hat{a}_i$. We use $\langle \ldots \rangle$ to denote nearest neighboring sites. In equation (4.1), the first term describes the kinetic energy of the system with hopping coefficient J; the second term is associated to the local chemical potential μ_i at site i; the last term is the dipole-dipole interaction with V the strength of the nearest-neighbors repulsive interaction energy when the dipoles are oriented perpendicular to the lattice plane, $r_{ij} = |\mathbf{r}_i - \mathbf{r}_j| = |(x_{ij}, y_{ij})|$ is the relative distance between site i and site j, θ and ϕ are the polar and azimuthal angle, respectively. Within this work, the dipoles are aligned parallel to each other and tilted out to the lattice plane using an external field. The azimuthal angle is fixed to $\phi = 45°$. We specify that, in agreement with [1], we consider all the energies in units of hopping amplitude J. Moreover, as customary in this field, the results are reported in units of k_B and $\hbar$. In their work, Y. Hebib, C. Zhang and B. Capogrosso Sansone studied the zero temperature properties of the system modeled by (4.1) and built the ground state phase diagram in the θ-V plane (see figure 3.3).

The question that we want to answer within this thesis is the following: how does the phase diagram studied in [1] change at finite temperature? In this chapter, we present our numerical analysis of the instability region, i.e. the region of the phase diagram found in [1] for $\theta \gtrsim 62°$. We also study the melting of the checkerboard phase as a function of the temperature.

4.1 Instability Region

In [1], it is reported the zero temperature phase diagram of the system at half filling, i.e. for a filling factor $n = 0.5$. The filling factor n is an important observable in this context and it is defined as the ratio between the average number of particles and the number of sites in the system. More formally we have

$$n = \frac{\langle N \rangle}{N_{site}} = \frac{\langle N \rangle}{L^2} = \frac{1}{\beta L^2} \frac{\partial}{\partial \mu} \ln \Xi, \tag{4.2}$$

where L is the linear size of the square lattice, μ is the chemical potential and

$$\Xi = \mathrm{Tr}\Big(\exp\left(-\beta \hat{H}_{DLB}\right)\Big)$$

is the grand canonical partition function. In the case of hard-core bosons (i.e. at most one particle per lattice site) the filling factor is limited to $0 \leq n \leq 1$.

The authors of [1] showed that, at $T = 0$, for $\theta \gtrsim 62°$, the system enters an *instability region.* For this range of parameters no filling factor other than $n = 0$ and $n = 1$ are stable and the system undergoes a first order transition between a fully filled ($n = 1$) and an empty filled ($n = 0$) lattice as a function of the chemical potential. Outside the instability region $n = 0.5$ is stable and the system can be found in different quantum phases, such as superfluid (SF), checkerboard solid (CB) and diagonal stripe solid (DSS), based on the values of the parameters θ and V.

It is interesting to understand whether and how the behavior of the system in the instability region of the phase diagram changes in response to an increase of temperature. We extend previous results by studying not only the stability-instability transition for $n = 0.5$, but also the stability of other filling factors $n \in [0, 1]$. In the following, we define the instability region as the set of points of the phase diagram in which not all filling factors are stable and, thus, in which we observe a first order phase transition between two non consecutive values on n by varying μ.

Let us first summarize the properties of a first order phase transition. A phase transition is the transformation of a physical system from a state of matter to another driven by changes in the parameters governing the system. In 1933, Paul Ehrenfest proposed a possible classification of phase transitions based on the continuity of the derivatives of the thermodynamic potential of the systems (the free energy F in the framework of canonical ensemble and the grand potential Ω for the grand canonical ensemble) at the critical point, i.e. in the point of the parameter space in which the transition occurs. The criterion state that: *"the order of the* *lowest derivative of the thermodynamic potential characterizing the system showing a discontinuity at criticality is the order of the phase transition".* It follows, that a first order phase transition is a transition in which the first derivatives of F and Ω, such as the entropy, the volume and the average particles number, are discontinuous functions of the thermodynamic variables, entailing an exchange of latent heat between the system and the environment during the process. Moreover, the discontinuous behavior of first order phase transitions is typically enriched by the presence of hysteresis. This phenomenon occurs because the system becomes trapped in metastable states (i.e. states associated with relative minima of the thermodynamic potential) due to barriers, causing the transition to happen at different values of the control parameter (e.g. T, μ) depending on whether it is increased or decreased. In the following, we will exploit the properties of first order phase transitions to determine the behavior of the system close to the instability region for $T > 0$.

In our analysis we fix the strength of the dipolar interaction to $V = 8J$, and study the behavior of the system for different values of the temperature. For each T, we consider different values of θ and analyze how the filling factor behaves as a function of the chemical potential. Practically, we give a set of parameters, such as $(T/J, V/J, \theta, \mu/J)$, as input of numerical simulations. Then, for each set of input parameters, the simulations outputs, among other observables, the average and actual (i.e. instant for that Monte Carlo configuration) number of particles.

The choice of n as the order parameter for our analysis has the following benefits. In quantum statistical mechanics, within the framework of the grand canonical ensemble, the grand potential Ω is related to the partition function of the system through the relation

$$\Omega = -\frac{1}{\beta} \ln \Xi, \tag{4.3}$$

it follows that by comparing the latter expression with the definition of the filling factor, i.e. equation (4.2), we can rewrite n in terms of the first derivative of the grand potential with respect to the chemical potential. Explicitly we get

$$n = \frac{\langle N \rangle}{L^2} = \frac{1}{\beta L^2} \frac{\partial}{\partial \mu} \ln \Xi = -\frac{1}{L^2} \frac{\partial}{\partial \mu} \Omega. \tag{4.4}$$

In this regard, as stated by Ehrenfest criterion, when the stystem undergoes a first order transition, the filling factor will present a discontinuous behavior with μ. Thanks to this property we can thus determine whether, for a certain set of parameters, the system belongs or not to the instability region by simply studying the profile of the filling factor as a function of the chemical potential. In fact, if, for a certain pair (θ_1, V_1), $n(\mu)$ shows a smooth behavior, we can state that all possible values of the filling factor are stable and that the point (θ_1, V_1) of the phase diagram does not belong to the instability region. If a pair (θ_2, V_2) leads to a discontinuous profile of $n(\mu)$, there exist some filling factors that cannot be achieved by the system because of the presence of a first order phase transition. In this case, the point (θ_2, V_2) would belong to the instability region.

We can now apply these ideas for different values of temperature.

4.1.1 Temperature $T = 5J$

We start with a system of linear size $L = 12$, and we vary the angle θ in the range $[65°, 85°]$. The plots of the profile of the filling factor as a function of the chemical potential are reported in figure 4.1.

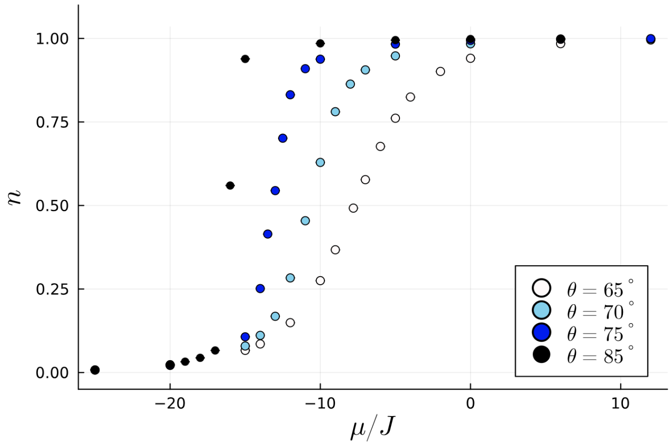

Figure 4.1: Profile of $n(\mu)$ for $T = 5J$, $L = 12$, $V = 8J$ and $\theta = 65°, 70°, 75°, 85°$ respectively in white, light blue, blue and black circles. Each dot is associated to a different Monte Carlo simulation.

As expected, for each angle, the filling factor is an increasing function of the chemical potential and it takes values in the interval $[0, 1]$. Moreover, we observe that, the larger the value of θ, the sharper the transition between filling factors. This behavior represents the hallmark of the approach of the system to the instability region. Figure 4.1 suggests that for values of θ lower than $75°$ the filling factor presents a smooth behavior and that all values of n can be achieved by the system. On the other hand, further analysis is needed for a correct interpretation of the behavior of the system for angles larger than $75°$. We want to understand if, regardless of the steepness of the curve $n(\mu)$, all filling factors are stable or a first order transition occurs.

In order to clarify these points and to avoid possible finite size effects, we have performed a new set of simulations for a system of size $L = 24$. We start with the analysis of the system for $\theta = 85°$. The reason behind this choice is to reduce the number of simulations, since if we find a smooth behavior of the filling factor with the chemical potential for that angle, then we can certainly state that all the angles $\theta \leq 85°$ do not belong to the instability region. The results of the simulations for $\theta = 85°$ and $L = 24$ are reported in figure 4.2.

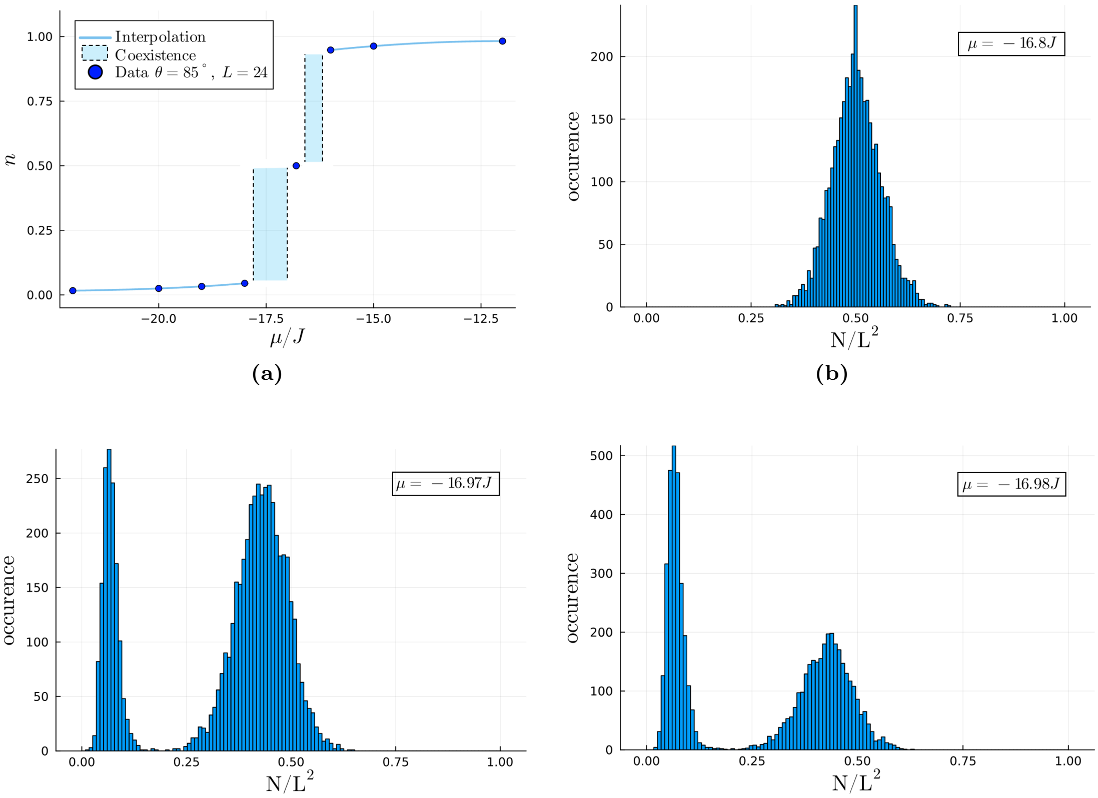

(a) **(b)**

(c) **(d)**

Figure 4.2: In panel (a) is reported the behavior of the filling factor for $T = 5J$, $L = 24$, $V = 8J$ and $\theta = 85°$. The dots correspond to the results of the simulations, the blue curves are the polynomial interpolation of the data and the blue regions indicate phase coexistence. In panel (b), (c) and (d) are shown the histograms of the occurrences of the normalized number of particles trapped in the lattice for a large number of MC configurations for respectively $\mu = -16.8J$, $\mu = -16.97J$ and $\mu = -16.98J$.

Panel (a) shows the profile of the filling factor as a function of the chemical potential. The pairs (μ, n) represented with a circle are stable points in which the system can be found, while the blue regions indicate the ranges of chemical potential for which phase coexistence is observed because of the presence of a first order phase transition. In order to understand this concept let us consider the images reported in panel (b), (c) and (d) of figure 4.2. The three plots represent, for a given values of μ, the histogram of the occurrences of the normalized number of particles in the lattice for a large number of Monte Carlo configurations.

The histogram in panel (b), which refers to $\mu = -16.8J$, presents a single peak centered in $N/L^2 \sim 0.5$. This feature allows us to conclude that the corresponding filling factor is stable since it results from the average of multiple values of normalized particles number with a single peak probability distribution. It follows, that for $\theta = 85°$, $n \sim 0.5$ is stable and it is thus possible to find the system at half filling for a small range of chemical potential.

On the other hand, the histograms referring to $\mu = -16.97J$ and $\mu = -16.98J$ (see respectively panel (c) and (d)), are characterized by two peaks, one of them centered in $N/L^2 \sim 0.05$ while the other in $N/L^2 \sim 0.5$. The peaks of the histograms correspond to minima of the grand potential Ω and the observed behavior is the hallmark of a first order phase transition. The presence of a double peak in the probability distribution of the number of particles observed in equilibrium Monte Carlo configurations is consistent with a scenario where two competing minima of the grand potential are present and the system evolves back and forth between these two minima in which it remains for a finite simulation time. The longer the system spends in one minimum, the higher the corresponding peak in the histogram would be. It follows that for the range of chemical potential corresponding to the blue regions in the plot, the system experiences a first order phase transition where the phases associated with the two minima of the grand potential coexist. The possibility for the system of overcoming the energy barrier that divides the two minima is what makes these states metastable and leads to the impossibility for the simulated system to stay into one of the two minima without moving to the other after a finite time simulation. In our case, the two peaks centered in $N/L^2 \sim 0.05, 0.5$ indicate that no filling factors are stable in the interval $(0.05, 0.5)$ and the system goes form $n \sim 0.05$ to $n \sim 0.5$, and vice versa, by means of a first order transition by varying the chemical potential. The same behavior is observed also for slightly larger values of μ. No stable filling factor exists in the range $(0.5, 0.95)$ and the system undergoes a first order phase transition between $n \sim 0.5$ and $n \sim 0.95$.

By repeating the same analysis for different angles θ we discover that the same behavior characterizes the system also for $\theta = 80°$ and $\theta = 90°$. In this regard, we can state that, for all $\theta \gtrsim 80°$ the system presents an instability in which the only available filling factors are $n \sim 0.05$, $n \sim 0.5$ and $n \sim 0.95$. As a response to a variation of the chemical potential the system undergoes a first order phase transition between a stable phase at $n \sim 0.05$ and at $n \sim 0.5$ and between a stable phase at $n \sim 0.5$ and at $n \sim 0.95$. For this range of angles, all the other filling factors are unstable.

We notice that, in contrast to what happens in the instability region found in [1], where the system undergoes a first order phase transition between exactly $n = 0$ and exactly $n = 1$, in our simulations the system never reaches $n = 0$ and $n = 1$. This behavior is due to the fact that we are working for $T > 0$. Due to thermal fluctuations, higher energy levels are populated resulting in $n \gtrsim 0$ and $n \lesssim 1$.

Next, we focus on lower polar angles. We consider a system of size $L = 24$ with an angle of dipole orientation equal to $\theta = 75°$. The profile of the filling factor as a function of μ is reported in figure 4.3

In contrast to what observed for $\theta \gtrsim 80°$, the filling factor shows a smooth behavior with μ and is characterized by a single peak histogram. The absence

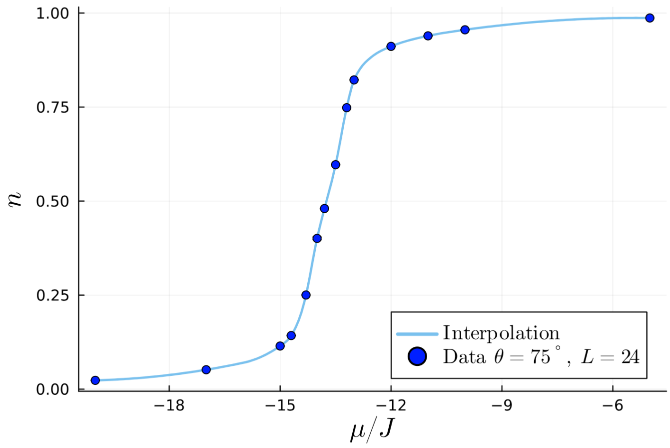

Figure 4.3: Profile of $n(\mu)$ for $T = 5J$, $L = 24$, $V = 8J$ and $\theta = 75°$. The dots correspond to the results of the simulations, while the blue curve is the polynomial interpolation of the quantum Monte Carlo data.

of first order transitions allows to consider the angle $\theta = 75°$ as a point outside the instability region. It follows, that for all the angles lower than 75° the whole range of filling factors $n \in [0, 1]$ is stable, and the system can be thus found in any possible n based on the value of μ.

In order to have a complete knowledge about the instability region at $T = 5J$, we need to investigate on the angles belonging to the region that goes from $\theta = 75°$ to $\theta = 80°$. In figure 4.4 we present the results obtained for $\theta = 78°$ and $L = 48$.

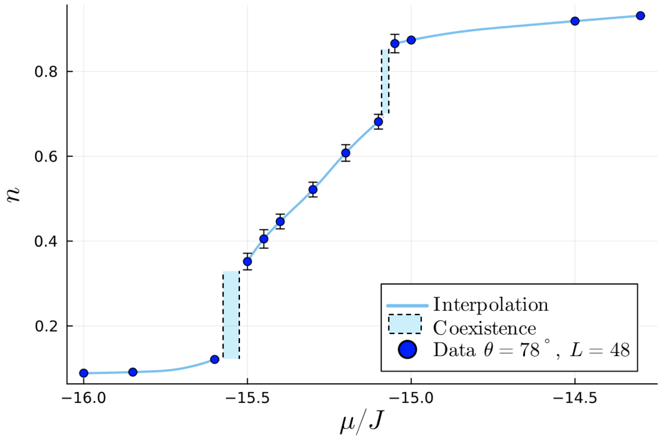

Figure 4.4: Profile of $n(\mu)$ for $T = 5J$, $L = 48$, $V = 8J$ and $\theta = 78°$. The dots correspond to the results of the simulations, the blue curves are the polynomial interpolation of the data and the blue regions indicate phase coexistence.

The profile of the filling factor reported in figure 4.4 acts like a cross between the one studied for $\theta = 75°$ and the one observed for $\theta = 85°$. Starting from low values of the chemical potential, the system is characterized by an almost vanishing filling factor $n \sim 0$, i.e. by an empty lattice configuration. As long as μ grows, we reach a critical value of chemical potential $\mu_1^* \sim -15.6J$ for which the system undergoes a first order phase transition from $n \sim 0.1$ to a value $n_1 \sim 0.35$, which fulfills the condition $0 < n_1 < 0.5$. Then, by further increasing the chemical potential the filling factor grows smoothly up to a certain value $n_2 \sim 0.68$, with $0.5 < n_2 < 1$, leading to an interval of stable filling factors $n \in [n_1, n_2]$. In correspondence to n_2 the system experiences a second critical point, $\mu_2^* \sim -15.1J$, in which a first order phase transition between n_2 and $n \sim 0.9$ occurs.

The latter results suggest that the smooth behavior of the filling factor observed for $\theta \lesssim 75°$ and the instability met for $\theta \gtrsim 80°$ are connected by an additional type of instability in which only a range of filling actors, i.e. $n \in [n_1, n_2]$, around $n \sim 0.5$ is stable and a first order transition arises when the system jumps between $n \sim 0.1$ and n_1 and between n_2 and $n \sim 0.9$. Moreover, the more θ tends toward 75°, the more we expect that n_1 and n_2 will, respectively, approach $n = 0$ and $n = 1$, while the more θ tends toward 80°, the more n_1 and n_2 will both approach $n = 0.5$.

The behavior of the system close to the instability region as a function of the angle θ, for fixed $V = 8J$ and $T = 5J$, can be summarized as follows. For $\theta \lesssim 75°$ the system is in the stability region in which no first order phase transition is observed and all filling factors can be achieved by the system. When $\theta \gtrsim 75°$ the system enters the instability region, since some of the values of n are no longer stable. Based on the results found for the angles belonging to the instability region, the latter can be divided into two distinct subregions. In the first, observed for $\theta \lesssim 80°$, the system is described by a phase that we can define as *intermediate instability*. For this range of angles, there exists an interval $[n_1, n_2]$, such that $0 < n_1 < 0.5 < n_2 < 1$, of stable filling factors, and we have found the presence of transitions of the first order between the filling factors at the boundaries of the stable interval and $n \sim 0.1, 0.9$. The width of the range $[n_1, n_2]$ depends on the value of θ we are considering. The second subregion, that arises for $\theta \gtrsim 80°$, is characterized by a much stronger instability where the system owns only three stable filling factors: $n \sim 0.05$, $n \sim 0.5$ and $n \sim 0.95$, and it jumps between them through a first order transition. For simplicity, we denote this kind of instability as *type-I instability.*

4.1.2 Temperature $T < 5J$

Let us now repeat the procedure performed for $T = 5J$ in the case of lower temperatures. As we shall see, the results obtained for $T = J, 2J, 3J$ are similar to those for $T = 5J$, but two interesting differences arise: firstly, a new type of instability is observed for large values of the angle θ and, secondly, the critical points of the transitions of the system from one phase to the other as θ increases moved towards lower angles.

$T = 3J$

For small angles, i.e. $\theta \lesssim 69°$, we recover a smooth behavior of the filling filling factor as a function of the chemical potential, entailing that the system belongs to the stability region. As the angles grow, i.e. $\theta \gtrsim 70°$ the system undergoes first order phase transitions, suggesting that the latter has reached the instability region. The behavior of the filling factor for growing values of θ inside the instability region is shown in figure 4.5.

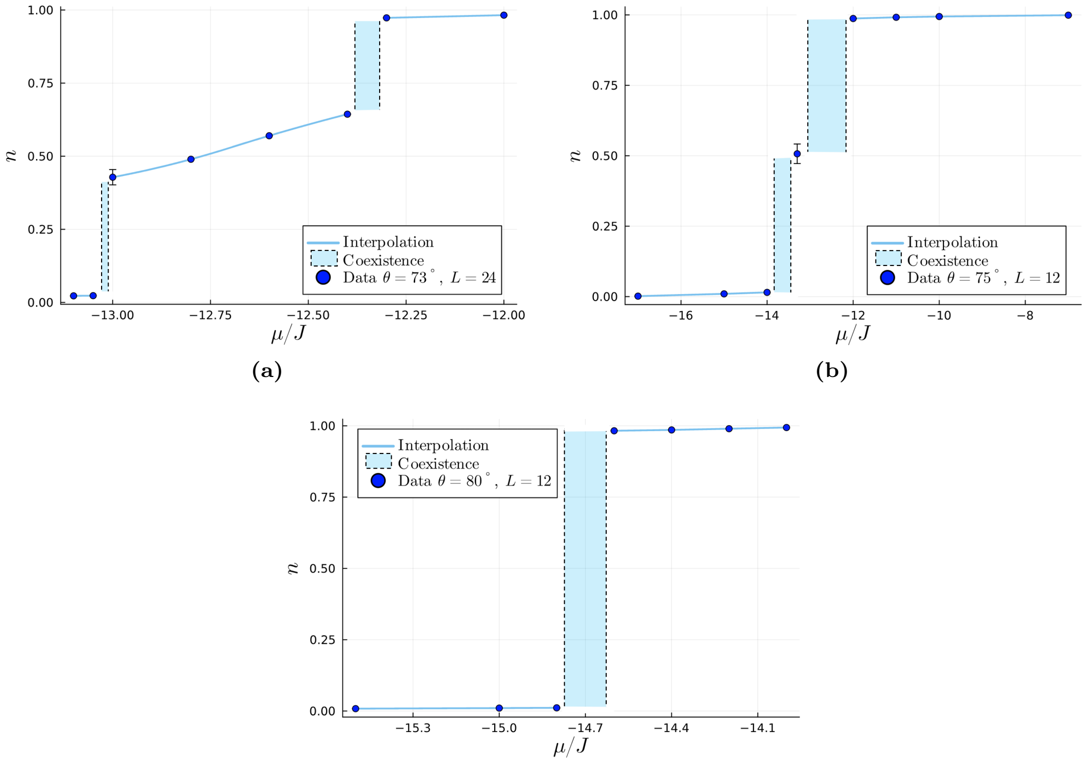

(a) **(b)**

(c)

Figure 4.5: Behavior of the filling factor as a function of the chemical potential in the instability region for $T = 3J$ and $V = 8J$. Panel a) shows the intermediate instability, panel b) the type-I instability and panel c) the type-II instability.

For angles $\theta \simeq 73°$ (panel (a)) the system is found in the phase we define as intermediate instability. In fact, there exists a small range of stable filling factors $[n_1, n_2] \sim [0.45, 0.65]$ that are connected to $n \sim 0$ and $n \sim 1$ by steep first order phase transitions. As we increase θ we recover, for $\theta \simeq 75°$ (panel (b)), type-I instability in which the system owns $n \sim 0$, $n \sim 0.5$ and $n \sim 1$ as the only stable values of filling factor. Due to the lower temperature, type-I instability does not hold up to $\theta = 90°$, but a further type of instability appears for large angles. When $\theta \gtrsim 80°$ (in figure 4.5 is reported the profile of n for $\theta = 80°$) half filling becomes unstable and the system jumps with a first order transition between an almost empty-filled lattice ($n \sim 0$) and an almost fully-filled lattice ($n \sim 1$). We define this region of the phase diagram in which only $n \sim 0$ and $n \sim 1$ are stable as *type-II instability* region. Notice, that type-II instability is the same kind of instability that is observed in [1].

$T = J$ and $T = 2J$

For $T = J$ and $T = 2J$ the system presents the same qualitative behavior as the one observed for $T = 3J$, but some quantitative differences are introduced. For lower temperatures, the critical point that divide the stability region from the instability one moves toward smaller values of θ. Moreover, the transition of the system from the intermediate instability region to the type-I instability region and from the type-I instability region to the type-II instability region occurs at smaller values of angles with respect to the one found for $T = 3J$.

4.1.3 Temperature $T > 5J$

We complete the analysis of the instability region by taking into account temperatures larger than $5J$. The reason behind this choice is the following. Our previous results highlight that the critical point dividing the stability from the instability region moves toward larger values of θ as long as we increase the temperature. In this regard, our aim is to find a sufficiently high values of T for which the instability region completely disappears. In the following we report the behavior of the system for $T = 8J$.

$T = 8J$

The profile of the filling factor for $\theta = 90°$ and $L = 36$ is shown in figure 4.6.

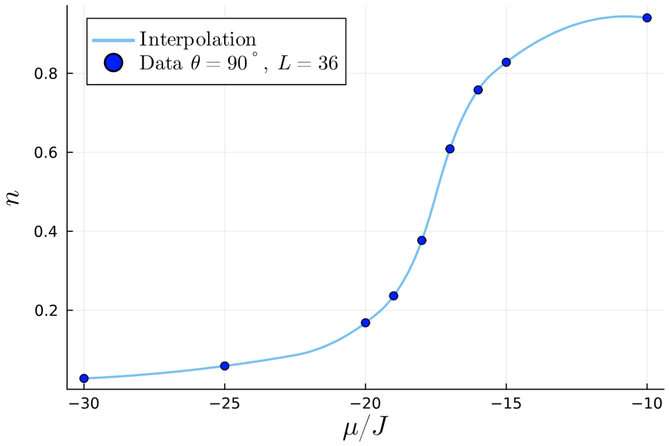

Figure 4.6: Profile of $n(\mu)$ for $T = 8J$, $L = 36$, $V = 8J$ and $\theta = 90°$. The dots correspond to the results of the simulations, while the blue curve is the polynomial interpolation of the quantum Monte Carlo data.

The smooth behavior of the filling factor suggests that, for all $\theta \leq 90°$, the entire range of filling factors is stable. For $T = 8J$ the instability region is no longer present.

The findings obtained for $T = 5J$ and for $T = 8J$ allow us to conclude that there exists a critical temperature $T_c \in [5J, 8J]$ for which the instability region completely disappears. In other words, for $T > T_c$ the system can take any possible value of the filling factor for all θ, while for $T < T_c$ there exists a critical value of the angle, $\theta_c(T)$, which divides the stability from the instability region.

4.1.4 Phase separation

The goal of this subsection is to present the arrangement of particles within the lattice when the system is inside the instability region. In type-II instability the system can have only densities equal to $n \sim 0$ and $n \sim 1$ since all the other filling factors are unstable. It follows, that the only configurations in which we can find the system within this region are: empty latte, i.e. no particle for each lattice well ($n \sim 0$), and fully filled lattice, i.e. one particle per site ($n \sim 1$).

For intermediate instability and type-I instability, the scenario is instead more interesting since there exist stable values of the filling factor that are different from $n \sim 0$ and $n \sim 1$. For all values of n that the system can take in these two subregions, we observe *phase separation.* In figure 4.7 we report the results obtained for $T = J$. In panel (a) of figure 4.7, we plot the behavior of the filling factor as a function of the chemical potential for $\theta = 65°$ for which the system belongs to the intermediate instability region. Panels (b),(c) and (d) display the density maps for three different values of n, i.e. $n \sim 0.4, 0.5, 0.7$, obtained for the same angle and temperature. A density map is a graphical representation of the local densities at the single sites of the lattice that allows us to detect the presence of a possible order in the system and thus the quantum phase characterizing it. Each circle of the density map corresponds to a different site of the optical lattice, and its radius is proportional to the local density at that site. As one can see in figure 4.7, for each stable filling factor inside the instability region the system is found in a phase separated state. In other words, the configuration that minimizes the grand potential for these sets of parameters is given by the segregation of the system into regions of different densities. A region of high density ($n = 1$) where the system behaves as an incompressible Mott-insulator, and a region of low density ($n = 0$) that we associate with vacuum.

The same phenomenon is observed also for all other values of temperatures analyzed in this work. As T increases the density maps still show phase separation. The boundaries between the empty and the fully occupied regions become less defined due to more enhanced thermal fluctuations.

4.1.5 Summary

Within our analysis, we were able to extend the results obtained in [1] for large θ for temperatures $T > 0$. For each value of T considered, we fix the strength of the dipolar interaction, $V = 8J$, and we study the behavior of the filling factor as a

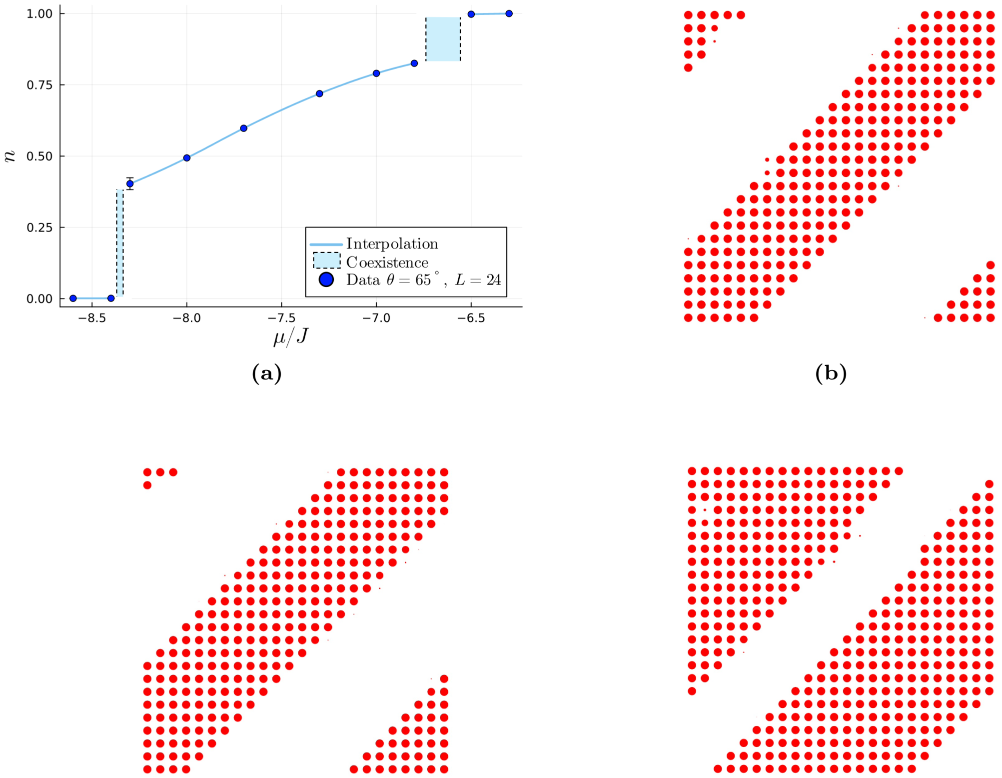

(a) **(b)**

(c) **(d)**

Figure 4.7: In panel (a) is reported the profile of the system density as a function of the chemical potential for $T = J$, $L = 24$, $V = 8J$ and $\theta = 65°$. In panel (b), (c) and (d) are reported the density maps for, respectively, $n \sim 0.4, 0.5, 0.7$ that shown the presence of phase separation in the system.

function of μ for different angles θ. In our work, we define the stability region as the range of θ for which all densities are stable, while the instability region is the region of the phase diagram where first order transition occurs. As expected, thermal fluctuations lead to a displacement of the critical point $\theta_c(T)$ toward larger values of θ. This behavior can be understood by considering the expression of the system Hamiltonian (4.1). The term modeling the dipolar interaction, because of the anisotropic nature of the latter, can make both positive and negative contribution to the total energy of the system as a function of the angle θ. On the one hand, when all dipoles are perpendicular to the lattice plane (i.e $\theta = 0$), the dipolar interaction is repulsive and gives a positive contribution to H. On the other hand, in the case in which all dipoles lie on the lattice plane (i.e. $\theta = 90°$), the interaction becomes attractive and contributes negatively to the total energy. In [1] they observed, thanks to MC simulations, that for $\theta_c(T = 0) \sim 62°$, the configurations that minimize the Hamiltonian are: no particles (i.e. $n = 0$) for $\mu < \mu^*$ and fully filled lattice (i.e. $n = 1$) for $\mu > \mu^*$. Where we indicate with μ^*

the critical value of chemical potential at which the transition occurs for $\theta \sim 62^\circ$. The same result, because of the functional form of the dipole-dipole interaction term, is observed for $\theta \gtrsim 62^\circ$, with the only difference that, the more θ grows, the more the energy gap between the ground state and the excited states increases. It follows, that if we consider two finite temperatures T_1 and T_2, such that $T_1 < T_2$, we expect that the critical angle will fulfill the relation

$$\theta_c(T_1) < \theta_c(T_2).$$

In fact, by allowing access to high energy levels, stronger thermal fluctuations lead to a reduction of the energy barrier between grand potential's energy minima. Therefore, we expect the instability region corresponding to lower θ to be destroyed by thermal fluctuations at lower temperatures.

For relatively small temperatures, i.e. $T = J, 2J, 3J$, the instability region is divided into three subregions. Starting from $\theta_c(T)$ the system is found in the intermediate instability region where, in addition to $n \sim 0$ and $n \sim 1$, there exists a range of stable filling factors around $n \sim 0.5$. The width of this interval decreases as we increase the angle, until we meet a specific value of θ for which the extremes of the interval collapse to $n \sim 0.5$ and the system enters in the phase we denoted as type-I instability. In this phase the system undergoes a first order phase transition between $n \sim 0$ and $n \sim 0.5$ and between $n \sim 0.5$ and $n \sim 1$, since all other densities are unstable. By further increasing θ the system reaches type-II instability that persists up to $\theta = 90^\circ$. In this region the only stable filing factors are zero and one.

For larger T, i.e $T = 5J$, the situation changes. The stronger thermal fluctuations completely destroy type-II instability. Finally, for sufficiently high temperatures, e.g. $T = 8J$, all the instabilities disappear. The profile of the filling factor as a function of the chemical potential is smooth for all θ.

Moreover, we were able to state that, for the sets of parameters belonging to the instability region and for $n \neq 0, 1$ the system shows phase separation for all the values of T.

4.2 CB - NF transition

In the following, we consider smaller values of the angle θ where for $T = 0$ the system is stable at half filling, i.e. $n = 0.5$. Our aim is to determine the critical temperatures for the melting of the quantum phases stabilized at zero temperature and half filling. To do so, we fix the temperature T and proceed as follows. We set $V = 8J$, the system size to $L = 12$ and we select different values of θ within the stable region. For each angle, we perform a fine tuning of the chemical potential in order to find the correct value of μ associated with a density $n = 0.5$, then, we simulate the behavior of the system for this set of parameters and characterize the quantum phase of the system for each value of θ by monitoring the superfluid stiffness ρ_s and the structure factor $S(\mathbf{k})$.

The superfluid stiffness is associated with the superfluid nature of the system. As we showed in chapter 2, the superfluid stiffness can be calculated in terms of the winding number through the relation

$$\rho_s = \frac{T}{d} L^{2-d} \left\langle \boldsymbol{\mathcal{W}}^2 \right\rangle , \tag{4.5}$$

where $\left\langle \boldsymbol{\mathcal{W}}^2 \right\rangle = \left\langle \sum_{i=1}^{d} \mathcal{W}_i^2 \right\rangle$ is the expectation value of winding number square and d is the dimension of the system (here $d = 2$). When the system is characterized by the off-diagonal long range order of the superfluid phase, then ρ_s is finite.

The structure factor characterizes diagonal long range order and it is defined as the Fourier transform of the density-density correlation function

$$S(\mathbf{k}) = \frac{1}{N} \sum_{\mathbf{r},\mathbf{r}'} \exp\left(i\mathbf{k} \cdot (\mathbf{r} - \mathbf{r}')\right) \langle \hat{n}_{\mathbf{r}} \hat{n}_{\mathbf{r}'} \rangle , \tag{4.6}$$

with N the total number of particles, $\mathbf{k}$ the reciprocal lattice vector, $\mathbf{r}$ the position vector and $\hat{n}_{\mathbf{r}}$ the number operator describing the density of particles in the lattice well in position $\mathbf{r}$. Peaks in the profile of S for certain values of $\mathbf{k}$ correspond to ordered phase in real space. As an example, $\mathbf{k} = (\pi, \pi)$ corresponds to checkerboard density pattern, while $\mathbf{k} = (\pi/2, \pi/2)$ corresponds to double diagonal stripe solid.

We now report the results obtained for $T = 5J$ and $T = J$.

4.2.1 Temperature $T = 5J$

The values of θ considered for $T = 5J$ are $\theta = 10°, 30°, 40°, 50°, 60°$. For each of them, we find that the system at half filling is described by an almost vanishing value of both ρ_s and $S(\mathbf{k})$ and by density maps characterized by what looks like random arrangements of particles.

These findings indicates that, strong thermal fluctuations completely destroyed the order of all the quantum phases observed at $T = 0$. It follows, that for $V = 8J$

and $T = 5J$, the system behaves as normal fluid for all values of θ belonging to the stability region.

4.2.2 Temperature $T = J$

For $T = J$ we focus on the checkerboard state. In [1] it is explained that, at $T = 0$ and $V = 8J$, the system undergoes a first order phase transition between CB and SF at a critical value of the angle $\theta_c(T = 0) \simeq 34.5°$. In this section, we will apply the procedure introduced before to determine how the behavior of the transition changes when T grows and to compute the critical value of the angle at which it occurs. Since we are working with a small value of temperature we expect that the critical point of the transition will not be too far away from the one found at $T = 0$. In this regard, we focus on angles $\theta \in [30°, 36°]$ and explore the behavior of the structure factor $S(\pi, \pi)$ and the superfluid stiffness ρ_s for this range of θ. Starting from $\theta = 30°$ and increasing the angle, we get a decreasing profile of $S(\pi, \pi)$ while ρ_s remains negligible. These findings allow us to obtain important information about the transition. On the one hand, the decreasing behavior of the structure factor is somehow an expected result since we are dealing with a transition from a CB phase, where $S(\pi, \pi)$ is large, to a phase characterized by zero value of $S(\pi, \pi)$ because of the absence of the diagonal long range order. On the other hand, the negligible value of the superfluid stiffness suggests that for $T = J$ the superfluid phase has already been destroyed by thermal fluctuations and a normal fluid state arises in its place. We thus discover, that in the range $\theta \in [30°, 36°]$ the first order CB - SF transition observed in the ground state is replaced by a different type of transition between checkerboard phase and normal fluid at $T = J$.

The disappearance of the CB order in favor of a normal fluid for this range of angles belongs to a second order phase transition of the same universality class as a two-dimensional Ising transition. In this context, it is possible to compute the critical value $\theta_c(T = J)$ of the transition using standard finite size scaling. In order to understand this idea let us focus on the behavior of the order parameter $S(\pi, \pi)$ as a function of θ. For systems of finite size, there are no "true" transitions, but simply smooth crossovers in which the order parameter goes from a finite value to a vanishing value by varying the control parameter. To extrapolate this behavior in the thermodynamic limit, i.e. $L \to \infty$, and thus to find the critical point of the transition, we need to exploit finite size scaling.

The main idea behind finite size scaling is that, close to the critical point of the transition, the correlation length ξ diverges as

$$\xi \sim |\theta - \theta_c|^{-\nu}, \tag{4.7}$$

where the exponent ν is called critical exponent and whose value depends on the universality class of the transition. For simplicity, we denote the critical point $\theta_c(T = J)$ with θ_c. However, since with quantum Monte Carlo simulations we deal with finite size systems, the correlation length cannot be larger than L. It follows, that the critical behavior of the system depends on the ratio L/ξ. This concept leads to the famous scaling hypothesis

$$S(\pi, \pi; \theta, L) = L^{-2\beta/\nu} f\big((\theta - \theta_c)L^{1/\nu}\big) \qquad \text{for} \quad |\theta - \theta_c| << 1 \tag{4.8}$$

that allows to write the scaling factor close to criticality in terms of a power law prefactor $L^{-2\beta/\nu}$, where β is another critical exponent, and a scaling function f. If we multiply both side of equation (4.8) by $L^{2\beta/\nu}$ we obtain

$$S(\pi, \pi; \theta, L)L^{2\beta/\nu} = f\big((\theta - \theta_c)L^{1/\nu}\big), \tag{4.9}$$

that at criticality becomes

$$S(\pi, \pi; \theta_c, L)L^{2\beta/\nu} = f(0), \tag{4.10}$$

namely a constant number independent of the system size.

In other words, we understand, that if we are far from criticality the behavior of $SL^{2\beta/\nu}$ will depend on the size of the system, while at criticality it becomes independent of L, i.e. it is said scale invariant. This result is crucial and allows us to determine the critical point of the transition. In fact, if we represent on the same plot the profile of $SL^{2\beta/\nu}$ as a function of θ for different values of L, then, since the quantity is scale invariant at criticality, all the curves will cross in correspondence of the critical point of the transition. The x-coordinate of the crossing point is exactly $\theta_c(T = J)$.

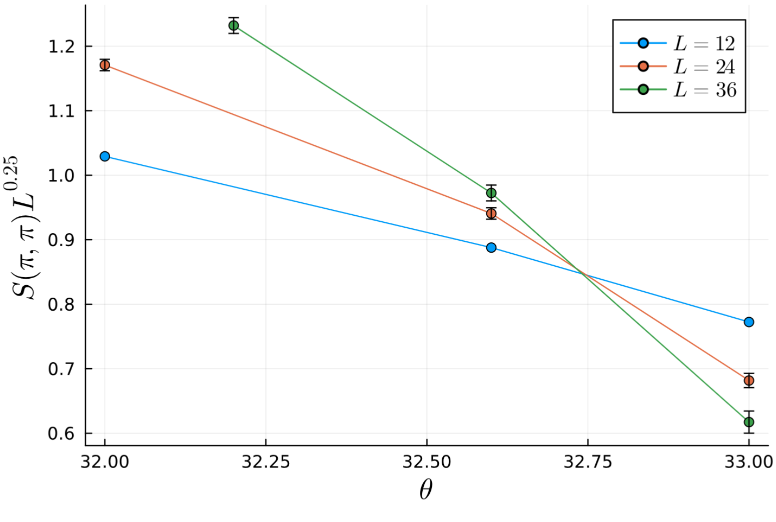

Figure 4.8: Scaled structure factor with $2\beta/\nu = 0.25$ as a function of θ for $L = 12, 24, 36$. The crossing determines the critical angle $\theta_c(T = J) = 32.74° \pm 0.05°$.

In figure 4.8 we plot the behavior of the scaled structure factor $SL^{2\beta/\nu}$, with critical exponent for the two-dimensional Ising universality class $2\beta/\nu = 0.25$, as a function of θ for $L = 12, 24, 36$. The crossing indicates the critical angle $\theta_c(T = J) = 32.74° \pm 0.05°$.

We observe that, as expected, the critical value of the transition moves toward lower values of θ as T increases. The CB region in the phase diagram will shrink as long as the temperature grows until we reach a sufficiently high value of temperature for which it disappears altogether in favor of a normal fluid.

Chapter 5

Conclusion and Outlook

In this work, we investigated the effects of finite temperature on a two-dimensional system of dipolar hard-core bosons. Starting from the zero temperature phase diagram presented in [1] we studied the melting of the checkerboard and superfluid phase, and the effect of thermal fluctuations on the instability region.

The response of the **checkerboard-superfluid transition** to thermal fluctuations was as expected. We observed that, by increasing the temperature, the superfluid phase is first destroyed, while the checkerboard is more robust and can hold up to higher temperatures. Moreover, we found that as the temperature increases, checkerboard melts in favor of a normal fluid at smaller values of polar angle θ.

We showed that the physical behavior of the **instability region** is strongly influenced by temperature. Interestingly, at low temperatures, the instability region is divided into three different subregions:

(i) the **intermediate instability region**: for polar angles belonging to this region, there exists a range of stable filling factors within an interval $[n_1, n_2]$, with $0 < n_1 < 0.5 < n_2 < 1$. First order phase transitions arise between the filling factor at the extremes of the stable interval and the values $n \sim 0, 1$;

(ii) the **type-I instability region**, where the only stable filling factors are $n \sim 0$, $n \sim 0.5$ and $n \sim 1$ and the system experiences a first order phase transition between them. All other densities are unstable and cannot be taken by the system;

(iii) the **type-II instability region**, in which the system undergoes a first order transition between an empty ($n = 0$) and a fully filled ($n = 1$) lattice as a function of the chemical potential.

As the temperature increases, stronger thermal fluctuations completely destroyed type-II instability, and the instability region is thus only composed of the two remaining subregions. Finally, for sufficiently high temperatures, all types of instability disappear. Moreover, we showed that, within the instability region, for all T, the system is found to be in a phase separation state.

The results obtained in this thesis allow us to reproduce a sketch of the finite temperature behavior of the instability region, as shown in figure 5.1. Further simulations are needed to make these predictions quantitative.

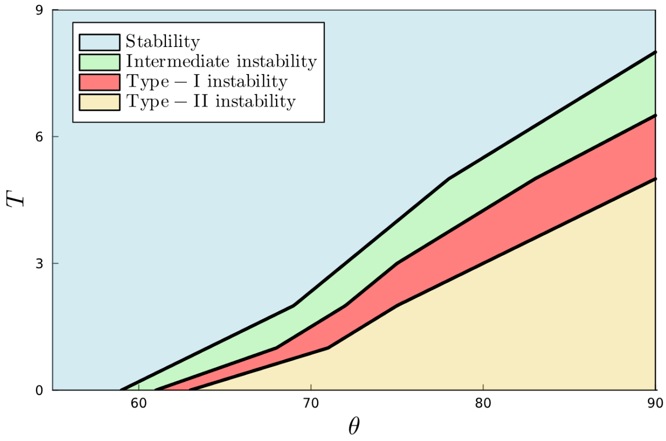

Figure 5.1: Qualitative instability diagram of the system for large θ.

From the results obtained in this dissertation, the potential applications of the instability diagram are clear. Firstly, our results can be used to correctly interpret experimental data as the one reported in [2]. More specifically, our findings suggest that some of the experimental results from [2] do not refer to the ground state as claimed. Moreover, once quantitative predictions are ready, we propose to use the instability diagram as a sort of thermometer. In fact, from experimental observation of certain stable filling factors, we can deduce the range of temperatures corresponding to the experimental system. This information is precious, since determining the true temperature in ultracold gas experiments remains a challenging task.

Bibliography

[1] Y. Hebib, C. Zhang, and B. Capogrosso Sansone. “Quantum Phases and Instabilities in Anisotropic Dipolar Lattice Bosons”. Manuscript in preparation.

[2] Lin Su et al. “Dipolar quantum solids emerging in a Hubbard quantum simulator”. In: *Nature* 622.7984 (Oct. 2023), pp. 724–729.

[3] Sébastien Balibar. “The Discovery of Superfluidity”. In: *Journal of Low Temperature Physics* 146 (Mar. 2007), pp. 441–470.

[4] P. Kapitza. “Viscosity of Liquid Helium below the λ-Point”. In: *Nature* 141.3558 (Jan. 1938), p. 74.

[5] J. F. Allen and A. D. Misener. “Flow of Liquid Helium II”. In: *Nature* 141.3558 (Jan. 1938), p. 75.

[6] S. N. Bose. “Planck’s Law and Light Quantum Hypothesis”. In: *Zeitschrift für Physik* 26 (1924), pp. 178–181.

[7] L. Landau. “Theory of the Superfluidity of Helium II”. In: *Phys. Rev.* 60 (4 Aug. 1941), pp. 356–358.

[8] Oliver Penrose and Lars Onsager. “Bose-Einstein Condensation and Liquid Helium”. In: *Phys. Rev.* 104 (3 Nov. 1956), pp. 576–584.

[9] J. Bardeen, L. N. Cooper, and J. R. Schrieffer. “Theory of Superconductivity”. In: *Phys. Rev.* 108 (5 Dec. 1957), pp. 1175–1204.

[10] M. H. Anderson et al. “Observation of Bose-Einstein Condensation in a Dilute Atomic Vapor”. In: *Science* 269 (July 1995), pp. 198–201.

[11] K. B. Davis et al. “Bose-Einstein Condensation in a Gas of Sodium Atoms”. In: *Phys. Rev. Lett.* 75 (22 Nov. 1995), pp. 3969–3973.

[12] Axel Griesmaier. “Generation of a dipolar Bose–Einstein condensate”. In: *Journal of Physics B: Atomic, Molecular and Optical Physics* 40.14 (July 2007), R91.

[13] Mingwu Lu et al. “Strongly Dipolar Bose-Einstein Condensate of Dysprosium”. In: *Phys. Rev. Lett.* 107 (19 Oct. 2011), p. 190401.

[14] Lev Pitaevskii and Sandro Stringari. *Bose-Einstein Condensation and Superfluidity.* Oxford University Press, Jan. 2016.

[15] Immanuel Bloch, Jean Dalibard, and Wilhelm Zwerger. “Many-body physics with ultracold gases”. In: *Rev. Mod. Phys.* 80 (3 July 2008), pp. 885–964.

[16] V. I. Yukalov. “Cold bosons in optical lattices”. In: *Laser Physics* 19.1 (Jan. 2009), pp. 1–110.

[17] B. Capogrosso-Sansone. “Quantum Monte Carlo study of ultracold bosons in optical lattices”. PhD thesis. University of Massachusetts, 2008.

[18] H. A. Gersch and G. C. Knollman. “Quantum Cell Model for Bosons”. In: *Phys. Rev.* 129 (2 Jan. 1963), pp. 959–967.

[19] J. A. Dunningham, K. Burnett, and Stephen M. Barnett. “Interferometry below the Standard Quantum Limit with Bose-Einstein Condensates”. In: *Phys. Rev. Lett.* 89 (15 Sept. 2002), p. 150401.

[20] D Jaksch. “Optical lattices, ultracold atoms and quantum information processing”. In: *Contemporary Physics* 45.5 (Sept. 2004), pp. 367–381.

[21] Maciej Lewenstein et al. “Ultracold atomic gases in optical lattices: mimicking condensed matter physics and beyond”. In: *Advances in Physics* 56.2 (Mar. 2007), pp. 243–379.

[22] N. V. Prokof’ev, B. V. Svistunov, and I. S. Tupitsyn. “Exact, complete, and universal continuous-time worldline Monte Carlo approach to the statistics of discrete quantum systems”. In: *Journal of Experimental and Theoretical Physics* 87.2 (Aug. 1998), pp. 310–321.

[23] Lev Davidovich Landau and Evgenii Mikhailovich Lifshitz. *Quantum mechanics: Non-Relativistic Theory.* Vol. 3. Elsevier, Oct. 2013.

[24] Ph. Courteille et al. “Observation of a Feshbach Resonance in Cold Atom Scattering”. In: *Phys. Rev. Lett.* 81 (1 July 1998), pp. 69–72.

[25] Markus Greiner et al. “Quantum phase transition from a superfluid to a Mott insulator in a gas of ultracold atoms”. In: *Nature* 415.6867 (Jan. 2002), pp. 39–44.

[26] Neil W Ashcroft and N David Mermin. *Solid State Physics.* Saunders College, 1976.

[27] Keiichi Edagawa. “Photonic crystals, amorphous materials, and quasicrystals”. In: *Science and Technology of Advanced Materials* 15.3 (June 2014), p. 034805.

[28] Matthew P. A. Fisher et al. “Boson localization and the superfluid-insulator transition”. In: *Phys. Rev. B* 40 (1 July 1989), pp. 546–570.

[29] Jiangyong Yu et al. “Two-dimensional Bose-Hubbard model for helium on graphene”. In: *Phys. Rev. B* 103 (23 June 2021), p. 235414.

[30] C. Bruder, R. Fazio, and G. Schön. “The Bose-Hubbard model: from Josephson junction arrays to optical lattices”. In: *Annalen der Physik* 517.9-10 (2005), pp. 566–577.

[31] Stasyuk, Velychko, and Vorobyov. “Phonon-like excitations in the two-state Bose-Hubbard model”. In: *Condensed Matter Physics* 18.4 (Dec. 2015), p. 43004.

[32] D. Jaksch et al. “Cold Bosonic Atoms in Optical Lattices”. In: *Phys. Rev. Lett.* 81 (15 Oct. 1998), pp. 3108–3111.

[33] D. van Oosten, P. van der Straten, and H. T. C. Stoof. “Quantum phases in an optical lattice”. In: *Phys. Rev. A* 63 (5 Apr. 2001), p. 053601.

[34] Anne van Otterlo et al. “Quantum phase transitions of interacting bosons and the supersolid phase”. In: *Phys. Rev. B* 52 (22 Dec. 1995), pp. 16176–16186.

[35] K. Sengupta and N. Dupuis. “Mott-insulator to superfluid transition in the Bose-Hubbard model: A strong-coupling approach”. In: *Phys. Rev. A* 71 (3 Mar. 2005), p. 033629.

[36] N. Elstner and H. Monien. “Dynamics and thermodynamics of the Bose-Hubbard model”. In: *Phys. Rev. B* 59 (19 May 1999), pp. 12184–12187.

[37] Barbara Capogrosso-Sansone et al. “Monte Carlo study of the two-dimensional Bose-Hubbard model”. In: *Phys. Rev. A* 77 (1 Jan. 2008), p. 015602.

[38] Yasuyuki Kato and Naoki Kawashima. “Quantum Monte Carlo method for the Bose-Hubbard model with harmonic confining potential”. In: *Phys. Rev. E* 79 (2 Feb. 2009), p. 021104.

[39] Stefan Wessel et al. “Quantum Monte Carlo simulations of confined bosonic atoms in optical lattices”. In: *Phys. Rev. A* 70 (5 Nov. 2004), p. 053615.

[40] T. D. Kühner and H. Monien. “Phases of the one-dimensional Bose-Hubbard model”. In: *Phys. Rev. B* 58 (22 Dec. 1998), R14741–R14744.

[41] Matteo Rizzi et al. “Phase Diagram of Spin-1 Bosons on One-Dimensional Lattices”. In: *Phys. Rev. Lett.* 95 (24 Dec. 2005), p. 240404.

[42] Omjyoti Dutta et al. “Non-standard Hubbard models in optical lattices: a review”. In: *Reports on Progress in Physics* 78.6 (May 2015), p. 066001.

[43] N. Prokof’ev. *Classical Monte Carlo and Metropolis Algorithm.* University of Massachusetts Amherst. Lecture Notes.

[44] Nicholas Metropolis et al. “Equation of State Calculations by Fast Computing Machines”. eng. In: *The Journal of Chemical Physics* 21.6 (1953), pp. 1087–1092.

[45] W. K. Hastings. “Monte Carlo sampling methods using Markov chains and their applications”. In: *Biometrika* 57.1 (Apr. 1970), pp. 97–109.

[46] F. Lingua. *The Monte Carlo Method: An analysis on Worm Algorithm Quantum Monte Carlo.* Politecnico di Torino. Work related to his PhD exam. 2014.

[47] F Lingua et al. “Multiworm algorithm quantum Monte Carlo”. In: *Physica Scripta* 93.10 (Sept. 2018), p. 105402.

[48] E. L. Pollock and D. M. Ceperley. “Path-integral computation of superfluid densities”. In: *Phys. Rev. B* 36 (16 Dec. 1987), pp. 8343–8352.

[49] N. Prokof’ev. *Classical Worm algorithm (WA).* University of Massachusetts Amherst. Lecture Notes.

[50] V. G. Rousseau. “Superfluid density in continuous and discrete spaces: Avoiding misconceptions”. In: *Phys. Rev. B* 90 (13 Oct. 2014), p. 134503.

[51] L. Santos. *Theory of dipolar gases.* Leibniz University Hannover. Lecture Notes.

[52] J. Werner et al. “Observation of Feshbach Resonances in an Ultracold Gas of ^{52}Cr”. In: *Phys. Rev. Lett.* 94 (18 May 2005), p. 183201.

[53] D. L Kovrizhin, G. Venketeswara Pai, and S Sinha. “Density wave and supersolid phases of correlated bosons in an optical lattice”. In: *Europhysics Letters (EPL)* 72.2 (Oct. 2005), pp. 162–168.

[54] Sudip Sinha and Subhasis Sinha. “Supersolid phases of bosons”. In: *Journal of Physics: Condensed Matter* (Aug. 2025).

[55] Davide Rossini and Rosario Fazio. “Phase diagram of the extended Bose–Hubbard model”. In: *New Journal of Physics* 14.6 (June 2012), p. 065012.

[56] D. Grimmer et al. *Quantum Phases of Soft-Core Dipolar Bosons in Optical Lattices.* 2014.

[57] C Zhang et al. “Equilibrium phases of tilted dipolar lattice bosons”. In: *New Journal of Physics* 17.12 (Dec. 2015), p. 123014.

[58] B. Capogrosso-Sansone et al. “Quantum Phases of Cold Polar Molecules in 2D Optical Lattices”. In: *Phys. Rev. Lett.* 104 (12 Mar. 2010), p. 125301.

[59] C. Zhang, A. Safavi-Naini, and B. Capogrosso-Sansone. “Equilibrium phases of dipolar lattice bosons in the presence of random diagonal disorder”. In: *Phys. Rev. A* 97 (1 Jan. 2018), p. 013615.

[60] A Safavi-Naini et al. “Quantum phases of dipolar bosons in bilayer geometry”. In: *New Journal of Physics* 15.1 (Jan. 2013), p. 013036.

[61] Chao Zhang et al. “Dipolar bosons in a twisted bilayer geometry”. In: *Phys. Rev. B* 111 (2 Jan. 2025), p. 024511.

[62] M. Guglielmino, V. Penna, and B. Capogrosso-Sansone. “Mott-insulator to superfluid transition in Bose-Bose mixtures in a two-dimensional lattice”. In: *Phys. Rev. A* 82 (2 Aug. 2010), p. 021601.

[63] F. Lingua et al. “Demixing effects in mixtures of two bosonic species”. In: *Phys. Rev. A* 92 (5 Nov. 2015), p. 053610.